EXPERIMENTAL INVESTIGATION OF INDUCED SEISMICITY IN GRANITIC ROCK ON CENTIMETER SCALE

Linus Villiger

**Faculty of Industrial Engineering, Mechanical Engineering and Computer Science
University of Iceland
2015**

EXPERIMENTAL INVESTIGATION OF INDUCED SEISMICITY IN GRANITIC ROCK ON CENTIMETER SCALE

Linus Villiger

30 ECTS thesis submitted in partial fulfillment of a
Magister Scientiarum degree in Innovative Sustainable Energy
Engineering

Advisor(s)
Prof. Dr. Halldór Pálsson (University of Iceland)
Prof. Dr. Rúnar Unnþórsson (University of Iceland)
Dr. Claudio Madonna (ETH Zurich)
Dr. Valentin Gischig (ETH Zurich)
Prof. Dr. Stefan Wiemer (ETH Zurich)

Faculty Representative
Prof. Dr. Halldór Pálsson (University of Iceland)

Faculty of Industrial Engineering, Mechanical
Engineering and Computer Science
University of Iceland
Reykjavik, September 2015

EXPERIMENTAL INVESTIGATION OF INDUCED SEISMICITY IN GRANITIC
ROCK ON CENTIMETER SCALE
EXPERIMENTAL INVESTIGATION OF INDUCED SEISMICITY
30 ECTS thesis submitted in partial fulfillment of a *Magister Scientiarum* degree in
Innovative Sustainable Energy Engineering

Faculty of Industrial Engineering, Mechanical Engineering and Computer Science
School of Engineering and Natural Sciences
University of Iceland
Hjardarhagi 2-6
107, Reykjavik, Reykjavik
Iceland

Telephone: 525 4000

Abstract

Enhanced Geothermal Systems (EGS) permit the exploitation of geothermal energy in deep, dry and impermeable formations of the Earth's crust. To create permeability, fluids under high pressure are injected into these deep formations, causing injection-induced seismicity. If large-magnitude seismic events occur, they can lead to public nuisance and infrastructure damage. The desire to better understand the physical processes causing large-magnitude events, so that they can be avoided or mitigated, is the motivation of this thesis.

The main focus here is on the localization and the associated analysis of differential stress- and injection-induced seismic events on a laboratory scale. Granite samples were subjected to axial compression under confinement until shear failure occurred. Detected differential-stress induced small-scale seismic events, referred to as acoustic emissions (AE), were localized; these made microcrack initiation, fault nucleation, and fault propagation visible. Magnitude analysis of induced AE showed temporal b-value variation throughout the experiment. Also, AE were detected during fluid injection into uniaxially loaded, cylindrical granite samples until breakdown pressure was reached. Breakdown pressure was reached several times over multiple pressure cycles with the result that injectivity (i.e. pressure vs. injection rate) and radial strain increased with every repeated cycle. This provided evidence of irreversible deformation. Estimated b-values obtained over pressure cycles appeared to be of a similar range of magnitude. Temporal b-values over one pressure cycle show a decrease with increasing injection pressure and are lowest at breakdown pressure. Accuracy of localized induced AE was comparably low and the main reason for this turns out to be the poorly developed seismic velocity model required for localization: it does not adequately describe occurring heterogeneities and anisotropies due to microcracking or fluid injection.

Contents

List of Figures

List of Tables

Acknowledgements

1. Introduction

Geothermal heat flows through the earth's crust at an average global rate of $59\,mW/m^2$ (Tester, 2006). Until 1972 (pilot plant at Fenton Hill, New Mexico), conversion of geothermal heat into electrical energy involved only natural hydrothermal systems. Such systems require a naturally occurring geothermal resource with a sufficient supply of hot fluid in a tapped aquifer, high rock permeability and porosity. However, a vast potential for geothermal energy lies in areas with low thermal gradient, in dry and impermeable rock. Enhanced or engineered geothermal systems (EGS), as opposed to the naturally occurring hydrothermal systems, could economically provide useful amounts of geothermal energy in such areas.

In order to access this energy, a number of steps must be followed. First, two or more boreholes are drilled into a target rock mass (well depth 4000 m to 6000 m) at which sufficient high temperature ($> 180°C$) is available. Secondly, highly pressurised water is pumped into these deep wells to induce shear along pre-existing fractures or create new fractures in the target rock mass. This fracturing process leads to increased permeability of the rock mass between the boreholes. The stimulated rock mass volume can then be used as a heat exchanger. Finally, heat is extracted from the reservoir rock by circulating water between the injection and production borehole (Hirschberg S., 2015; Tester, 2006).

Fracturing processes during hydraulic stimulation can lead to induced seismic events. Most events are of low magnitude ($M_L < 2$, (Bachmann et al., 2011)), but the few high magnitude events can lead to public nuisance and infrastructural damage and hence to the termination of geothermal projects (e.g. M_L 3.2, EGS project in the city of Basel, (Bachmann et al., 2011)). However, economical considerations, such as geographic proximity to electrical energy and heat supply, lead to projects being initiated in densely populated regions (Kraft et al., 2014). Since new projects bear high risks in terms of induced seismicity and feasibility, EGS is far from being a standard technology in energy conversion. Presently, no heat exchanger has been successfully created.

When focusing on hydraulic stimulation, two main problems must be solved. (1) Efficient underground heat exchangers need to be engineered that can provide geothermal energy for decades, while at the same time (2) keeping the consequences of hydraulically induced seismicity at an acceptable level. A competence group embedded in the Swiss Competence Center for Energy Research (SCCER) at the Federal Institute of Technology (ETH) in Zurich was

formed to address these two problems. One main task of the group is to achieve a better understanding of seismic risk management during hydraulic stimulation. For this to occur, our grasp of the physical processes that lead to induced seismicity has to be improved. More precisely, spatial and temporal distribution, as well as statistical analyses of the magnitudes of occurring events in connection to pressure and fracture propagation, resp. orientation during fluid injection need to be comprehensively investigated (Research, 2015).

The above-mentioned scientific questions can be addressed on various scales ranging from laboratory (i.e. centimeter) to field scale (i.e. actual stimulation experiments). On one hand, small-scale experiments can be closely monitored and performed so as to allow maximum control of boundary conditions. Ramping experiments up in scale, on the other hand, leads to a reduction of monitoring options and controllability, even as the proximity to actual in-situ conditions improves. A large scale ($20\ m\ x\ 20\ m\ x\ 20\ m$) recently initiated and ongoing hydraulic-shearing experiment by SCCER on a natural fault at the Grimsel Test Side (GTS) is a step towards understanding the basic physical mechanisms involved. This Master's thesis however focuses on small-scale laboratory experiments.

Hydraulic stimulation is targeted at crystalline rock masses in the upper crust (10 to 15 km depth). It involves fault reactivation and fracturing, which are brittle phenomena that – on a small scale – involve microcrack initiation and coalescence. Microcracks in small-scale rock samples emit elastic waves called acoustic emission (AE). AE are normally detected using piezo-electric transducers attached to the sample. Experiments initiating a fracture by axial compression have been performed in the past and show an increasing AE rate close to failure (Holcomb, 1986). A milestone in recording, processing and interpreting AE is presented in the work of Lockner (1993). He performed differential stress-induced seismicity experiments under triaxial conditions and used a spatially distributed array of transducers which allowed him to locate the recorded AE. Knowing the location of an AE permits further statistical analyses based on the energy release of each AE. A recent study was performed by Lei et al. (2014) who repeated differential stress-induced seismicity experiments using state-of-the-art equipment (higher sampling rate, higher number of piezo-electric transducers) allowing a more precise location of events. Charalampidou et al. (2014) conducted experiments on hydraulically induced AE on a rock sample by reactivation of an artificially induced shear fault under triaxial conditions.

This thesis aims to explore AE acquisition and processing during differential stress-induced seismicity as well as during hydraulically induced seismicity on small-scale and intact granitic rock samples ($\sim\emptyset 60\ mm\ x\ 100\ mm$). Experiments conducted are the first research efforts in

the field of laboratory-scale acoustic emissions (AE) by the SCCER. Finding an optimal acquisition system, in addition to suitable processing software as well as anticipating problems connected to an accurate localization of AE are questions that are addressed in this work.

The experiments conducted in this project are divided into two parts. The first part describes the localization of AE and the problems associated with it. As a first test, pencil lead breakage (PLB) events were initiated and localized on a cylindrical, unloaded aluminum sample, which features a particularly straightforward homogeneous and isotropic seismic velocity distribution. Based on the acquired knowledge, two confined compression (triaxial compression) experiments (GR1, GR2) were conducted to describe AE in function of deformation. The experiments were performed at the "Laboratoire de Géologie de l'Ecole Normale Supérieur" (ESN) in Paris. Experiment GR1 was a classic triaxial compression experiment on a cylindrical rock sample. Under constant confining pressure, the axial compressive stress was increased at a constant rate until failure occurred. AE were counted during the experiment. Experiment GR2 was designed to induce a hydraulic shear failure on an intact sample. The sample was preloaded at the same confining pressure as in GR1 and at 90 % of the axial compressive stress that was required to initiate failure in experiment GR1. In case of the GR2 experiment, the intention was to induce failure by an increased pore pressure. Unfortunately, the sample failed as a result of an increased differential stress before it failed through pressure. However, the experiment was closely monitored, and as a result it still permitted localization and comprehensive analyses of AE in combination with local strains, confining and axial compressive pressure. Special focus was put on the process of localisation of acoustic events.

In the second part, an unconfined hydro-fracturing experiment (HF1) under uniaxial loading was performed at ETH Zurich. The purpose of the experiment was to increase permeability between an injection and a production borehole drilled 25 mm apart. AE were analysed as well as injection pressure, injection rate and radial strain.

This thesis begins with a theoretical introduction to rock mechanics and acoustic emission. The methodology chapter describes sample preparation, as well as details of the experimental apparatuses used, and also includes an analysis section, in which concepts for the interpretation of results are introduced. The subsequent result section details the two experimental main parts. The experimental findings are then discussed and finalised in a conclusion. A suggestion of possible future experiments, as well as requirements for equipment, are given at the end of the thesis.

2. Theoretical prerequisites

2.1. Mechanical properties of rock

Rock under upper crustal conditions generally deform in a brittle manner through fracturing and faulting. Requirement for a brittle failure is a certain critical stress level, which has to be reached. Microscopic fractures are then formed and coalesce between each other or stress is realised through frictional sliding along a pre-existing interface. Also frictional sliding requires the breakage of asperities and the fracturing of previously healed fault segments (Brantut et al., 2013).

Compared to mechanical properties of metals, crystalline rock, such as granite, has a much more complex behaviour under stress. A reason for this complex behaviour is that intact rock consists of an aggregate of minerals with different mechanical properties. In addition, pores and cracks are present. All these factors contribute to a heterogeneous, anisotropic and porous nature of intact rock.

Conducting an axial compression test under a constant applied strain rate to a cylindrical rock sample is the most common method of investigating the mechanical properties of rocks. The parameters of interest are elastic moduli, strength, seismic wave velocities, porosity, etc. If the mantle surface of the cylindrical sample is free of traction the compression is unconfined ($\sigma_1 > 0, \sigma_2 = \sigma_3 = 0$; Figure 2.1$a$), whereby σ_1 represents the maximum vertical, σ_2 the maximum horizontal and σ_3 the minimum horizontal principal stress in the system. Generally, in the field of Geology the convention $\sigma_1 \geq \sigma_2 \geq \sigma_3$ holds (Jaeger et al., 2007).

A triaxial compression is performed if stress is applied on cylinder mantle surface ($\sigma_1 > 0, \sigma_2 = \sigma_3 > 0$; Figure 2.1b). If a confined compression test is done on a cylinder the stresses in the two orthogonal directions perpendicular to the cylinder axis are equal. A so called true-triaxial compression test can be performed on a cubical sample ($\sigma_1 > \sigma_2 > \sigma_3 > 0$; Figure 2.1c) (Jaeger et al., 2007).
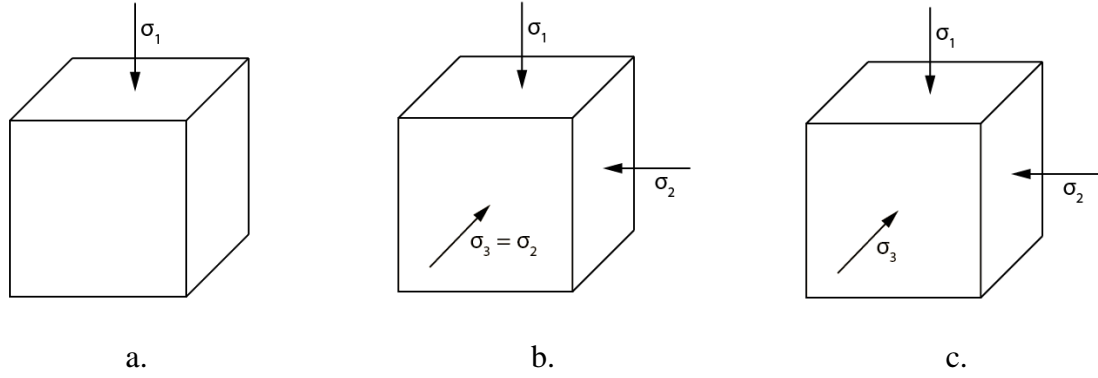
Figure 2.1: State of stress at an infinitesimal cube: Uniaxial stress (a), traditional triaxial stress in which the lateral principal stresses are the same (b), true-triaxial stress in which the three principal stresses are different (c) (modified after: Jaeger et al. (2007)).

Measuring axial and volumetric strain while compressing a cylindrical rock sample under triaxial conditions at a constant strain rate leads to a typical stress-strain behaviour shown in Figure 2.2. The convention used is that positive normal strain corresponds to a decrease in linear dimension of the sample.
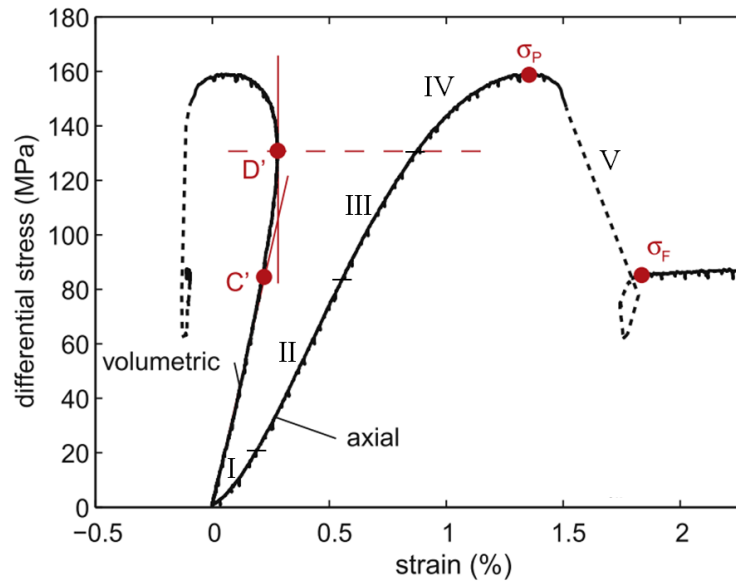
Figure 2.2: Stress-strain curve for Darley Dale sandstone deformed at a constant strain rate of $10^{-5}s^{-1}$ until failure. The sample was deformed under 30 MPa confining pressure. Differential stress corresponds to $\sigma_1 - \sigma_3$ (modified after: Brantut et al. (2013)).

The brittle failure process shown in Figure 2.2 can be broken down into a number of distinct stages. (I) First, the axial stress-strain curve shows an increasing slope additionally to a positive volumetric strain. Reason for this is the closure of pre-existing microcracks, a compaction of the rock sample, which leads to axial stiffening. The stiffening occurs in direction normal to loading. If confining pressure is high, this stage cannot be observed, because pre-existing microcracks are already closed through the applied confining stress before axial compression is initiated. (II) Secondly, an increasing stress leads to an almost linear increase in strain,

which means the rock deforms quasi-elastically. (III) The third stage starts at the point where the volumetric strain deviates from linearity and marks the onset of dilatancy (C'), which means it also marks the point of micro crack initiation and with it the onset of irreversible changes. Additionally, the slope of the axial stress-strain curve starts to decrease, which corresponds to stiffening of the rock sample. At D' the volumetric strain reaches its maximum, this point marks the transition from compaction dominated to dilatancy-dominated deformation. (IV) During stage four, the level of dilatant dominated cracking and volumetric strain increases. In this stage microcracks begin to coalesce to macroscopic cracks, which finally lead to a through going shear fault. Peak stress is achieved at σ_P. The through going fault is followed by dynamic failure of the rock sample (Figure 2.2, dashed line). In this case the failure is very hard to capture because the testing machine is more compliant than the rock sample. (V) Finally, stage five shows frictional sliding of the two parts along the generated shear fault, which is controlled by the residual frictional stress σ_F (Brantut et al., 2013).

2.2. Brittle deformation

Griffith (Jaeger et al., 2007) postulates that in homogenous, elastic and intact materials numerous submicroscopic flaws such as fluid inclusions, pores or just grain boundaries exist (Griffith microcracks). In theoretical studies, these flaws are represented as small, flattened ellipsoids. Applying tensile stress to the surroundings of a flaw leads to stress concentration at flaw boundaries, whereas the magnitude of the occurring stress exceeds the applied stress by far. This stress concentration is the reason why atomic bonds, which binding force is 10 to 1000 times greater than the tensile strength of the material, can be broken at comparably "low" applied loading. The magnitude of the stress concentration depends mainly on the shape, the position and the orientation of the flaw.

Microcracks propagate from the flaw tip in different, or in a combination of three different deformation modes (Figure 2.3).

Mode 1   Mode 2   Mode 3
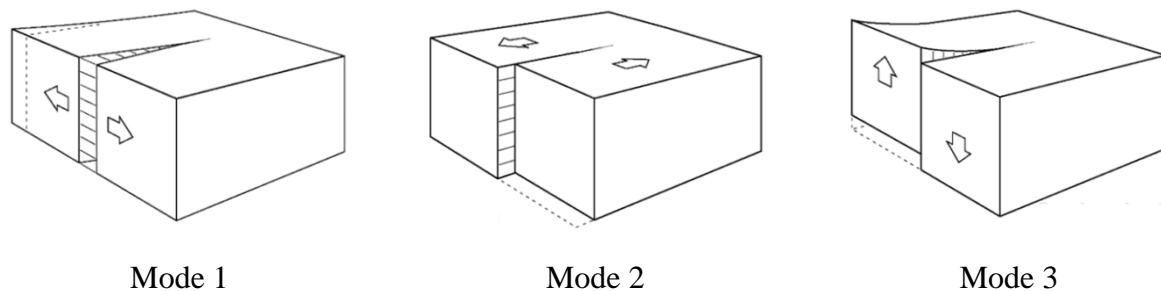
Figure 2.3: Crack-tip deformation modes (modified after: Burg (2015))

Mode 1 represents an opening mode fracture, which further propagates as a tensile fracture. Mode 2 is known as sliding mode fracture, which further propagates as shear fracture. Mode 3 is named tearing mode fracture. It propagates as shear fracture.

When local tension breaks the cohesion between atoms at the boundary of flaws, microcracks begin to propagate and, once micro-crack density is large enough, coalesce between each other. As a consequence of further increased loading macroscopic fractures lead to failure of the material (Burg, 2015). Finally, it must be noted that it is nearly impossible to predict the strength of a material based on theories of micro-crack formation and coalescence. However, the investigation of acoustic emission recorded during the formation of a macroscopic crack is one step in the direction of investigating micro-crack formation (more information on formation of microcracks in Section 2.4, acoustic emission).

Insight to the formation of macroscopic fractures is given by phenomenological/empirical fracture criteria, such as the Mohr-Coulomb failure criterion. Coulomb estimated what shear strength needs to be exceeded for a shear fracture to form on a plane of failure. Physically the cohesive binding forces additionally to the frictional forces between particles along a fracture plane need to be exceeded:

$$|\tau| = c + \mu\sigma_n \tag{1}$$

In Coulombs criterion τ and σ_n are applied shear and normal stress at an eventual fracture plane, c is the material constant of cohesion and μ represents the coefficient of internal friction. Both variables c and μ are not solely depending on the material, they are also highly dependent on surrounding conditions.

Later, Mohr confirmed through numerous experiments that the relationship between shear stress τ and normal stress σ_n, while introducing a fracture in a certain material is not linear as Coulomb predicts. σ_1, the applied maximal principal stress at failure increases at a less-than-linear rate with the minimal horizontal principal stress σ_3. However, loading conditions at failure of each experiment displayed in Mohr's circle are used to construct the failure envelope, which is unique in shape for every specific rock.
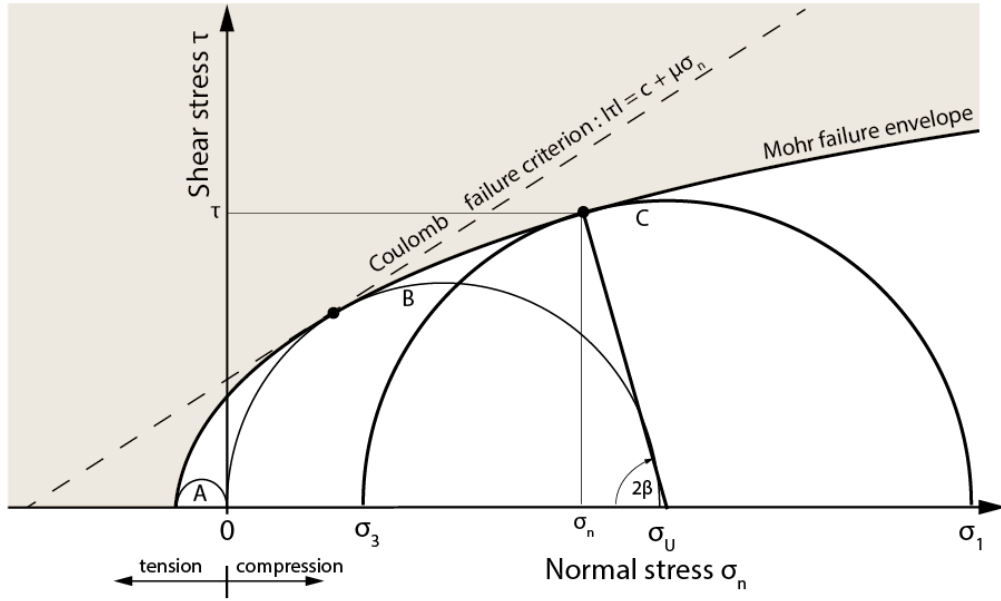
Figure 2.4: Failure envelope introduced by Mohr showing different loading conditions (A, B, C) at failure. The envelope separates the stable region to the unstable region (grey). Negative normal stress represents tension, positive values of normal stress correspond to compressional stress. (modified after:Burg (2015))

In Figure 2.4 different loading conditions at failure are shown. Figure 2.5 shows the corresponding fracture in a cylindrical sample.
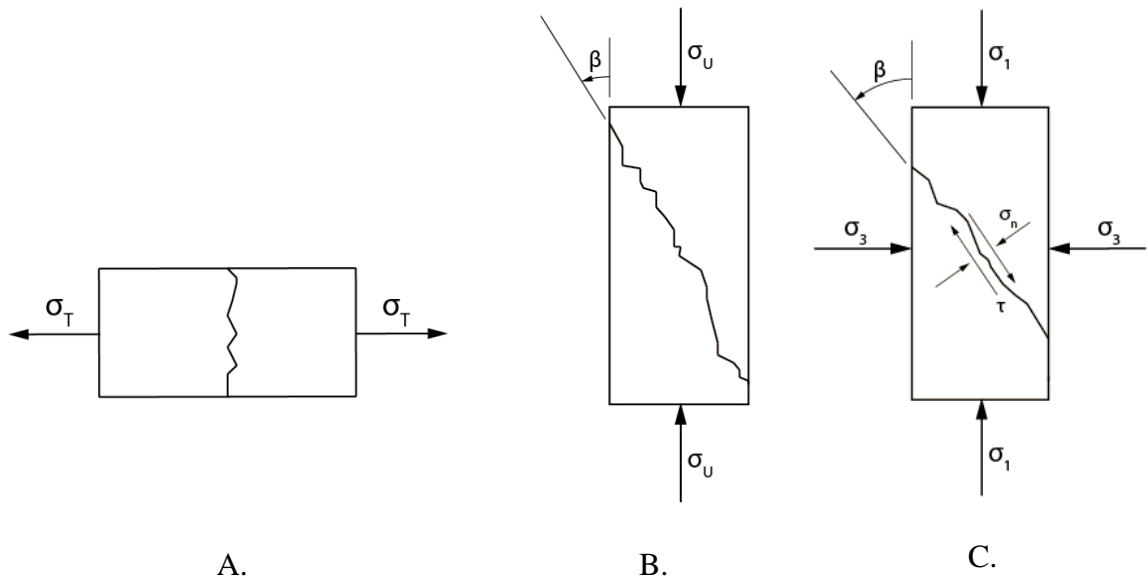
Figure 2.5: Induced fractures at different loading conditions. A. Tensile fracture, B. shear fracture under uniaxial compression, C. shear fracture under triaxial compression (modified after Lockner et al. (2002)).

Condition A leads to a tensile failure, which is oriented perpendicular to the maximum tensile stress. Loading condition B shows an induced shear fracture under uniaxial compression. Dependent on the uniaxial compressive stress σ_U, the fracture plane is typically inclined at an angle β in the range of 20° to 45°. Condition C represents a triaxial compression under axial compressive stress σ_1 and confining stress σ_3. Here, the inclination of the fracture plane is

also depending on the confining stress. Shear stress τ and normal stress σ_n represent the stress condition parallel resp. perpendicular to the fracture plane (Burg, 2015; Lockner et al., 2002). Generally, the prediction of the orientation of a fracture plane is difficult and does not only depend on the applied stress field. The texture of the rock mass plays a crucial role. Assuming isotropic and homogenous rock with random microcracks, grain boundaries and other small-scale weaknesses, the rock mass will find its own plane of failure according to the theory mentioned above (Jaeger et al., 2007).

It is important to take into consideration that Mohr's theory of failure is assuming that failure is controlled by the maximum principal stress and the minimum principal stress.

2.3. Effects of pore pressure

In the above section, failure of rock is described in cases where differential stress is acting on a rock sample. There is another effect, which plays a role when it comes to failure of rock. Because of its porous nature, rock volume is typically saturated with fluids. Generally, the pore fluid is water, but could also be oil, or gas, etc. Pore fluids can affect the failure of rock in two ways. On the one hand, the chemical interaction between fluids and rock can play a role, on the other hand purely mechanical effects of pore pressure can contribute to failure. This thesis emphasis lies on the enhancement or permeability creation in rock and therefore focuses on short-time and purely hydro-mechanical effects of pore pressure (Jaeger et al., 2007). Hydraulic stimulation of a rock volume foresees the artificially increase of pore pressure through pumps. Thereby an injection pressure is applied to a section of a bore hole. Depending on the prevailing stress field, the rock permeability and the viscosity, resp. the injection pressure of the fracturing fluid a new macroscopic shear or tension fracture is formed. As a third option, an existing fracture, if favourably oriented, can be reactivated by a comparable low pore pressure and brought to slip (Solberg et al., 1977).

Shear fracture in intact rock

In general, an increasing pore pressure, p_f, acts "outwards" and against the prevailing lithostatic pressure applied by the formation.

$$\sigma_{1*} = \sigma_1 - p_f$$
$$\sigma_{3*} = \sigma_3 - p_f$$

(2)

Here, σ_i^* represents the maximum horizontal and the minimum vertical principal stress under the influence of the pore fluid pressure. The stress field illustrated in Mohr's circle additionally to Mohr's failure envelope allows a schematic understanding of the influence of an increasing pore pressure (Figure 2.6).
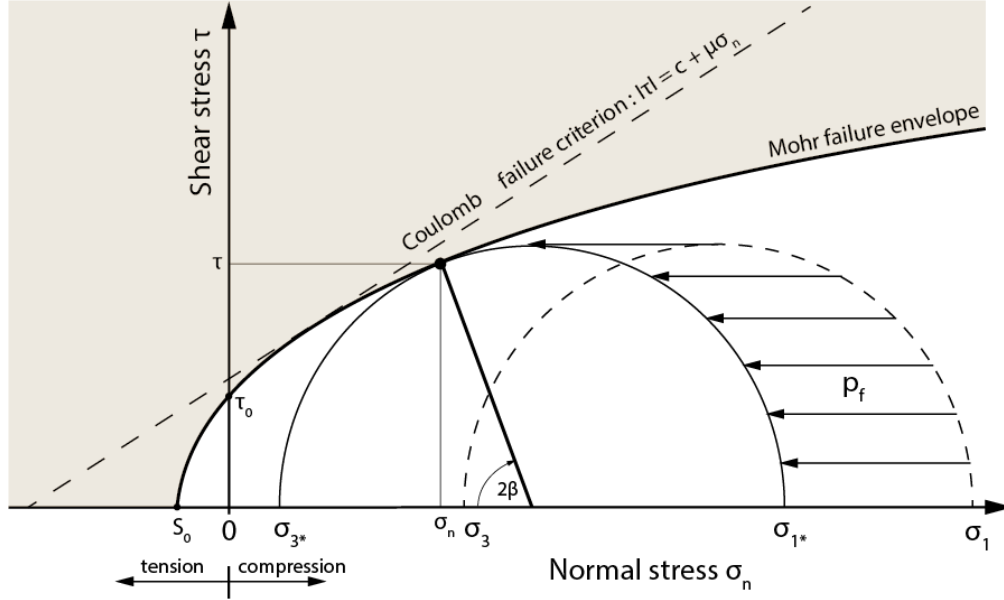
Figure 2.6: Initiated shear fracture in intact rock at an angle β as a result of an increased pore pressure. τ_0 is the required shear stress to overcome cohesion, whereas S_0 represents the tensile strength of the rock. (modified after: Burg (2015))

As can be seen in Figure 2.6, an increasing pore fluid pressure leads to a shift to the left of the prevailing stress field closer to the failure line. Because of this, also a "safe" in situ state of stress in the absence of pore pressure can fail if pore pressure is increased by a sufficient amount (Burg, 2015). It can also be seen, and it is experimentally approved (Solberg et al., 1977) that a shear fracture in intact rock is only formed if the prevailing differential stress $(\sigma_1 - \sigma_3)$ is sufficiently high. In nature shear fractures are formed in regions where significant tectonic stresses exist (Solberg et al., 1977).

Tension fracture in intact rock (hydraulic fracturing)

To initiate a tension fracture the injection pressure needs to exceed a certain break-down pressure. The magnitude of the break-down pressure depends on the tensile strength of the rock and the prevailing stress field. The pressure has typically to be higher than the minimal principal stress σ_3 (Preisig et al., 2015).

$$p_f > \sigma_3 \qquad (3)$$

Forming tension fractures are then oriented perpendicular to the minimal principal stress. Furthermore, it is expected (Preisig et al., 2015) that tension fractures will close again, when pressure is released, resulting in only a small net permeability increase.

Illustrated additionally to Mohr's failure envelope this leads to Figure 2.7.
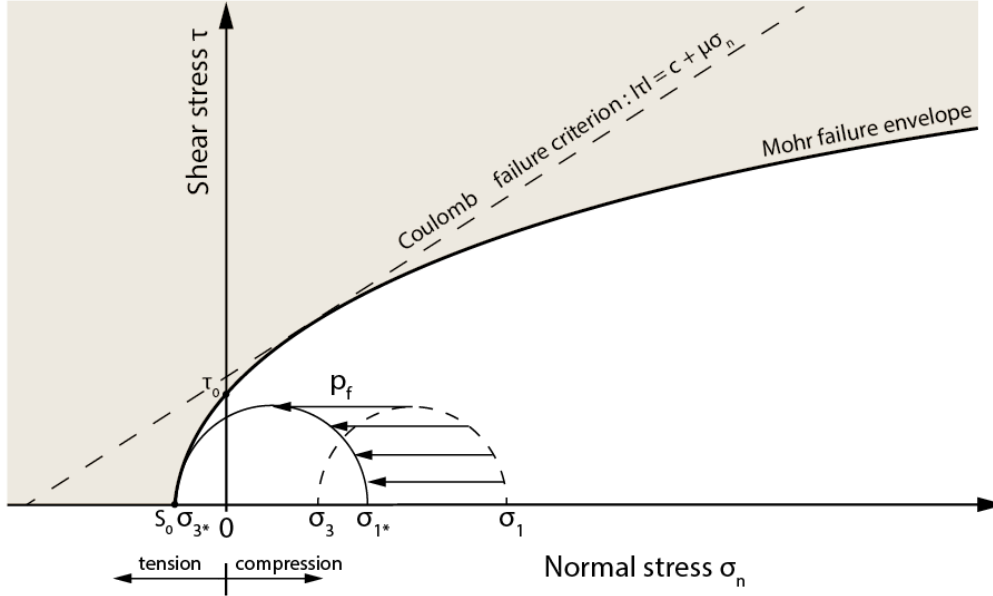
Figure 2.7: Induced tensile fracture by an increased pore pressure under a possible in situ stress field. τ_0 is the required shear stress to overcome cohesion, whereas S_0 represents the tensile strength of the rock. (modified after: Burg (2015))

Reactivation of shear fractures (hydraulic shearing)

In the case of the reactivation of shear fractures, also known as hydraulic shearing, the objective is to induce slip along pre-existing fractures. Hydraulic shearing assumes no cohesion along a rough fracture surface and can be expressed with Mohr-Coulomb's failure criterion.

$$|\tau| \geq \mu(\sigma_n - p_f) \tag{4}$$

Where τ is the applied shear stress parallel to the fracture plain, μ represents the coefficient of friction of the fracture and σ_n is the stress acting normal to the fracture plane. The pore pressure required to induce slip along an existing fracture plane is generally less than the minimal principal in situ stress σ_3 and certainly less than the pore pressure needed for hydraulic fracturing. As a requirement to allow slip a pre-existing fracture needs to be favourable oriented. Preisig et al. (2015) suggests an angle of 30° of the fracture plane to the maximum principal stress σ_1.

Compared to hydraulic tension fractures, hydraulic shearing is a self-propping mechanism because of the roughness and irregularity of the fracture surface, which leads to the permanent gain of aperture and fracture permeability (Preisig et al., 2015).

Finally, it is also suggested that in practice the two fracture mechanism hydraulic fracturing and hydraulic shearing often act to a varying degree in combination (Preisig et al., 2015).

2.4. Acoustic emission

As mentioned in the introduction, microcrack formation or frictional sliding in brittle behaving rock is connected to the rapid release of energy in the form of a transient elastic waves (i.e. acoustic emission). These waves are assumed to propagate from a point source through the material. An assembly of spatial distributed transducers (i.e. the transducer array) at the surface of a sample can be used to record the elastic wave as displacement and translate it to a voltage signal. These recorded signals provide information about size, location and deformation mechanism of the forming microcrack (Lockner, 1993). A minimum of four compressional wave (i.e. the P-wave) picks recorded at spatially distributed transducers are required to locate an event. In addition, a velocity model is needed which describes the actual seismic velocity distribution of the sample under investigation. The P-wave is the first wave arriving at the sensor. With some delay and often stronger amplitude, the shear wave (S-wave) arrives at the sensor. Detecting the onset of arriving waves is called picking. Picking the P-wave has the advantage that it arises from the noise level, whereas the S-wave is often superimposed by the foregoing P-wave (Barbara, 2005). Figure 2.8 shows an acoustic event recorded during the triaxial compression experiment GR2. The event lasted longer than $102,4\ us$ with a peak amplitude of $128\ mV$.
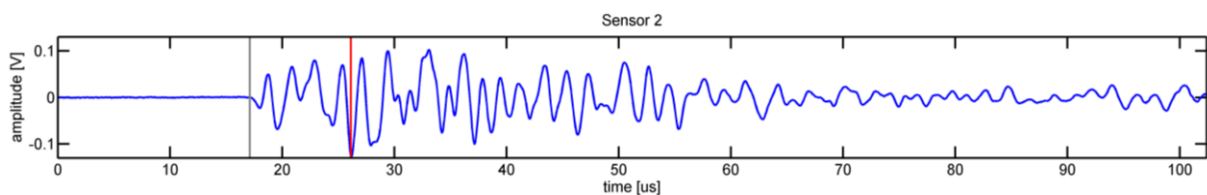
Figure 2.8: Acoustic event recorded over 1024 samples (102.4 us) at a sampling rate of 10 MHz. (vertical grey line: manual P-wave pick, vertical red line: peak amplitude)

The physical strength of seismic sources (i.e. earthquakes) is usually indicated in magnitudes. Estimating magnitudes presupposes measurements of ground motion and the known distance between measured ground motion and the source of the seismic event. Calculation of magnitudes can also be applied to small scale seismic sources (i.e. AE). Small scale ground motions are usually measured by piezo-electric transducers which are not calibrated. However, if the

source of an AE is known a magnitude can be assigned to it on an experiment specific relative scale. Adding up events with equal magnitudes in discrete bins leads to a cumulative frequency-magnitude distribution of the recorded events (Figure 2.9).
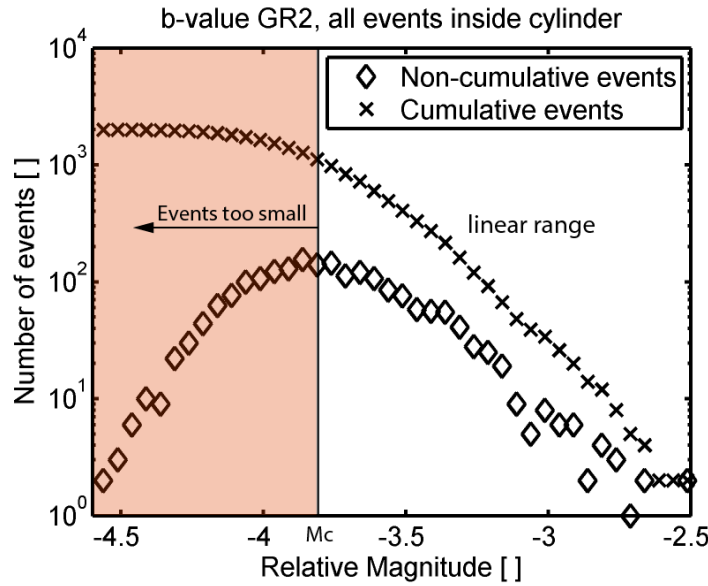
Figure 2.9: Example frequency-magnitude distribution of foreshocks localized inside the granite sample of the triaxial compression experiment GR2.

Using a log-plot, the cumulative frequency-magnitude distribution shows a descending gradient and a great portion of it is nearly linear. The magnitude data of the linear range is following a power law, the Gutenberg-Richter (GR) relationship.

The power law is typically used in earthquake seismology describing the magnitude distribution. The most common form is:

$$\log\big(N(M \geq M_i)\big) = a - bM_i \qquad (5)$$

whereas $N(M \geq M_i)$ represents the number of events with magnitudes greater than M_i. a and b-value are constants (Warner et al., 2003). The b-value is a relevant parameter for seismic hazard analysis. It represents the relative proportion of small vs. large events. High b-values represent an event catalogue with more low magnitude events compared to high magnitude events (and vice versa). The power law by GR can be applied to magnitudes in a time-space volume of own choosing (Goebel et al. (2013) suggest a catalogue size of at least 150 events). Also, temporal or spatial b-value mapping is possible.

Catalogues recorded in nature or on a laboratory scale are never complete at low magnitudes. The reasons are: (1) The event is too small to be detected by all receivers or the event is too small and a trigger threshold of data acquisition is not reached, (2) small events get superimposed by large events. The obtained event catalogue in Figure 2.9 is incomplete which is

shown by the decreasing number of low magnitude events. Estimating a magnitude of completeness (Mc) above in which 100 % of the events are detected is essential for a reliable estimation of b (Woessner, 2005) (more information in estimating Mc provided in Section 3.4.5).

Investigating controlling factors which affect seismicity in nature proves to be difficult because of the volumetric reach of fault zones. Earthquake catalogues are far from being complete, acting stresses and fault structures are to a large extend unknown. Because of this attempts have been made in order to discover analogies between closely monitored and controlled laboratory scale induced seismicity (AE) and earthquakes occurring in nature.

Brace et al. (1966) first suggested an analogy between shallow earthquakes and laboratory experiments, more precisely the mechanism of stick-slip during sliding along old or newly formed faults in the earth and stick-slip events which are frequently accompanied by frictional sliding. Lockner (1993) conducted a triaxial compression experiment on Westerly granite. Axial compression was continuously adjusted to maintain a constant AE-rate (a constant axial compression rate and a compliant loading frame would lead to abrupt and violent failure). Sources of recorded AE were localized (Figure 2.11).
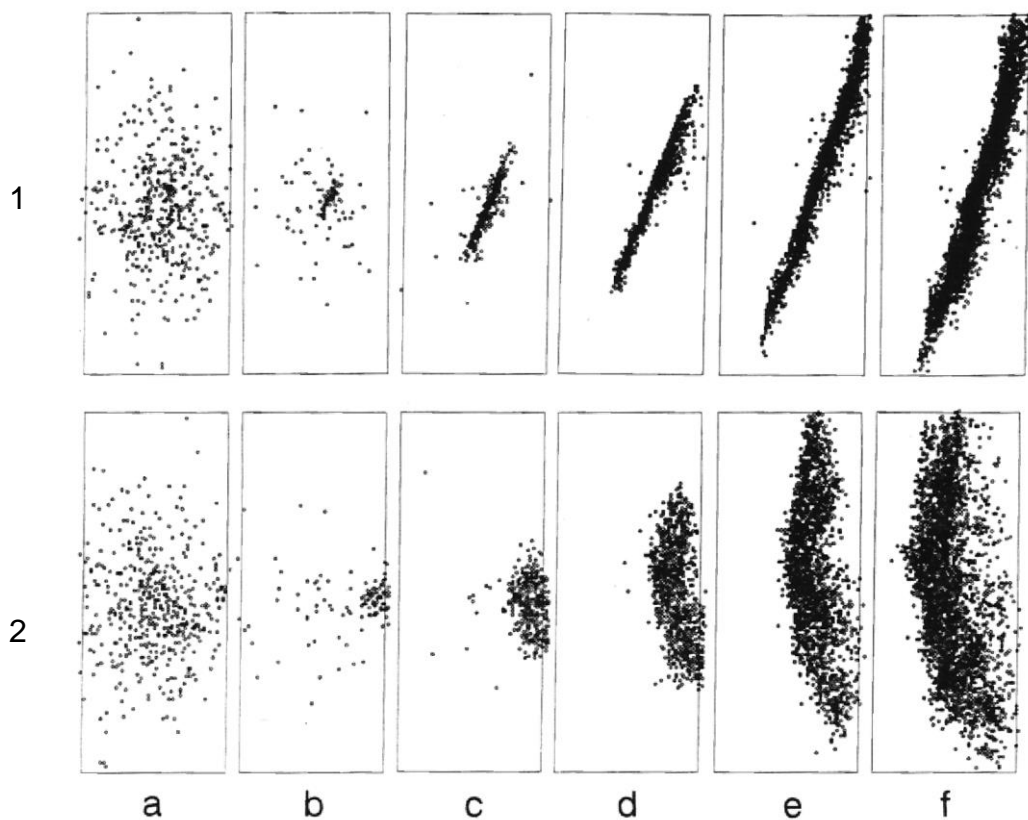
Figure 2.10: Localized AE of triaxial compression experiment shown in Figure 2.11.
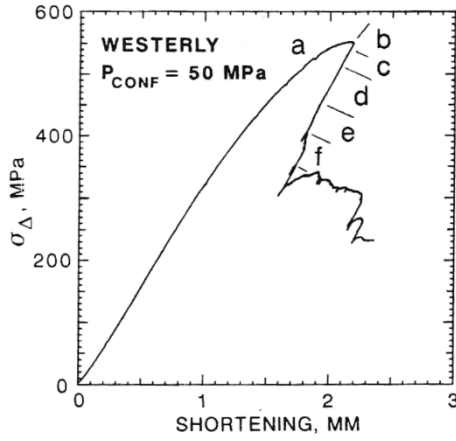
Figure 2.11: Complete shear fault formation during triaxial compression (sample size: $\emptyset\, 76.2\, mm\, x\, 190.5\, mm$). a) represents microcrack initiation, b) fault nucleation, from c) to f) the fault propagates. View [1] is along strike, view [2] reveals a plot turned 90° clockwise (modified after: Lockner (1991).

A recent work by Goebel et al. (2013) then focused on stick-slip laboratory experiments recording AE and investigating time dependent b-values. They showed that time dependent b-values mirror the stress build up and release during a stick-slip experiment. More importantly, it was shown that the amount of b value increase during a slip event of the experiment gives insights into the corresponding stress drop. This means that b-value variation in nature could eventually be used to approximate the stress state on a fault, which in turn could be used for a time-dependent seismic hazard assessment.

Charalampidou et al. (2014) focused more on the hydraulically induced seismicity side, investigating the reactivation of a shear failure plane (Section 2.3) due to fluid injection under a high compressive stress state on a laboratory scale. There, first motion polarities of the recorded AE were analysed, which allows to determine the occurring fracture modes (Section 2.2) during reactivation. Insights gained from the experiment could be important because it is assumed that during large scale hydraulic stimulation the mechanism of hydraulic shearing plays a significant role (McClure, 2014).

3. Methods and Materials

The experiments were performed at two different locations. Localization experiment in homogeneous-isotropic media and unconfined-hydrofracture experiments (HF1, HF2) were performed at ETH in Zurich. Triaxial compression experiments (GR1, GR2) were performed at the "Laboratoire de Géologie de l'Ecole Normale Supérieur" in Paris. At both locations acoustic emission acquisition systems manufactured by Applied Seismology Consultants (ASC) were employed.

3.1. Sample preparation

Rock samples used in this work, were coarse grained, granitic cores taken from the GTS at a depth of $400\ m$, in the Grimsel area in Switzerland. The Granite has a coarse grain texture and an average grain size of $1.5\ mm$. The reason for choosing this kind of granitic rock was due to an ongoing large scale hydraulic-shearing experiment at GTS. Also, permeability creation within an EGS project in Switzerland is targeted to comparable crystalline, granitic rock masses.
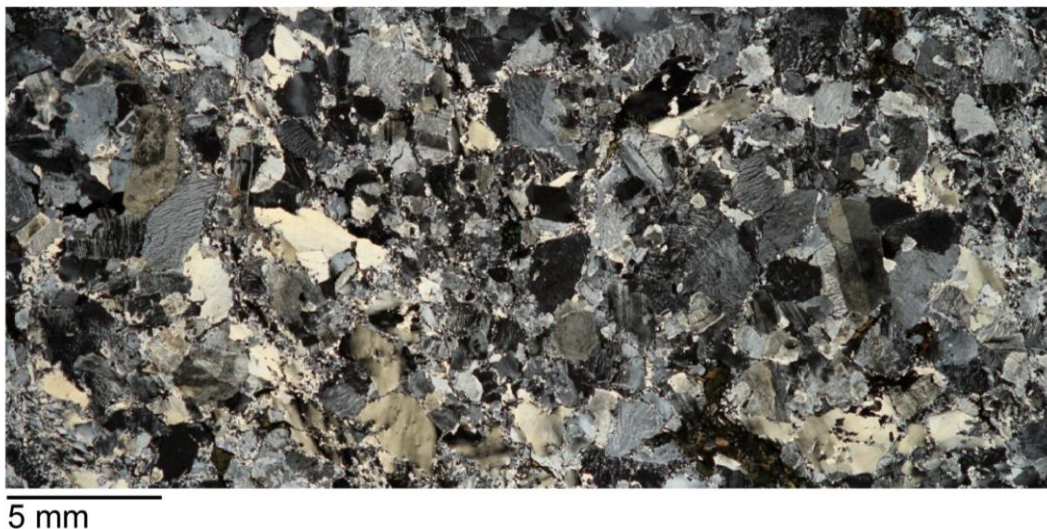
Figure 3.1: Thin section of Grimsel Granite (courtesy of Claudio Madonna).

3.1.1. Localization of AE in homogeneous-isotropic media

Localization experiments at ETH Zurich were performed on an aluminum cylinder ($\emptyset\ 76\ x\ 80\ mm$). The aluminum cylinder was equipped with four piezo electronic sensors (Glaser type, more information provided in Section 3.3.2). The sensors were screwed into sensor holders made of aluminum, which are glued by standard instant adhesive to the cylinder (Figure 3.2).
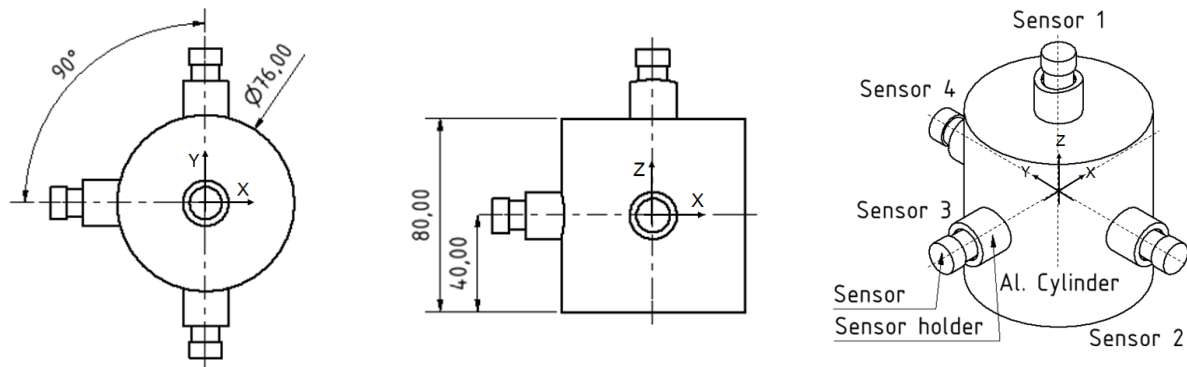
Figure 3.2: Cylindrical aluminum sample and sensor locations.

3.1.2. Confined compression experiments

To ensure a uniform stress distribution during the compression, parallelism and smoothness of the sample front surfaces is of great importance. The two granite samples were drilled using a $40\ mm$ core diameter drill bit. After sawing the cylindrical samples to a length of $88 +$ $0.2\ mm$, parallelism of the two front surfaces perpendicular to the cylindrical axis was ensured using a lathe. A sample holder made of steel with undercuts on both sides was used to simplify clamping and to ensure parallelism of both front surfaces (Figure 3.3).
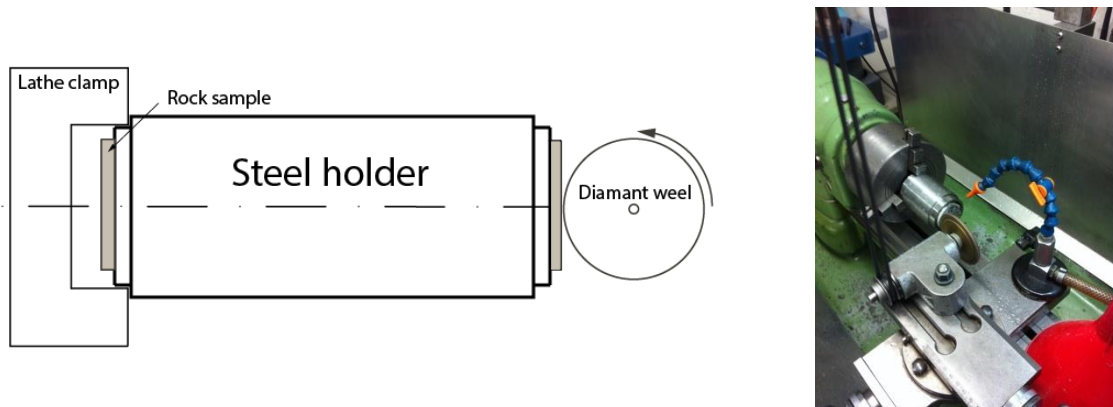
Figure 3.3: Lathe assembly, rotational direction of lathe should be in opposition compared to the rotational direction of the diamante wheel.

Practical experience shows best results at opposite direction of rotation between lathe and diamond wheel. It is most beneficial to start in the center of the surface area working outwards. Lathing the granite sample allows smooth front surface areas and an accuracy of parallelism of $\pm 10^{-2}\ mm$.

Four strain gauge patches (Tokyo Sokki, FCB-2-11) were glued (Tokyo Sokki, VH03F) to the sample (Figure 3.4). The patches were placed in the center of the sample, 90° apart from each other. The pins of the strain gauges were extended using wires ($0.08\ m^2, 0.44\ \Omega/m$), which were soldered to the strain gauge pins.

The Vieton-rubber jacked (inner diameter: 35 mm, length: 125 mm thickness: 5 mm) prevented the rock from oil contamination and was punctured using a 7 mm drift punch. During punctuation a PVC plastic core (diameter: 40 mm) was used to support the rubber jacket. Two small punctuations allowed a strain gauge wire feed trough (Figure 3.4).
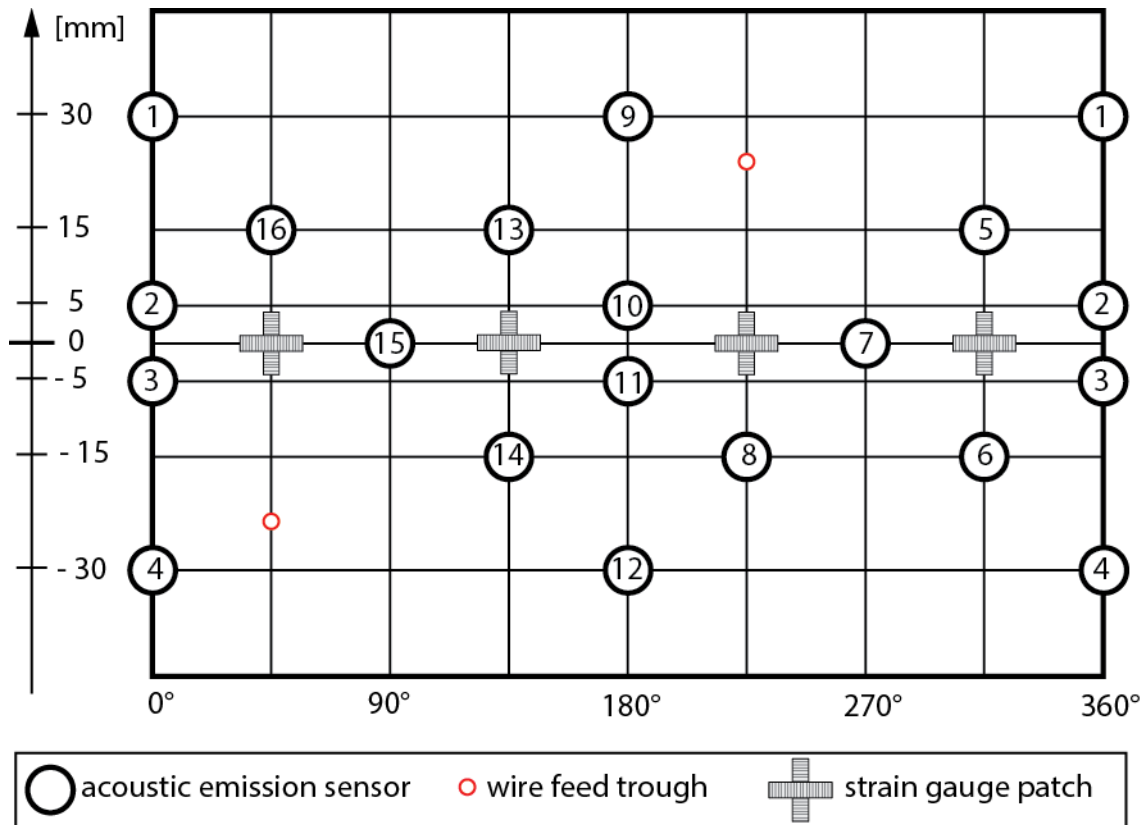
Figure 3.4: Development of transducer position, wire feed through and strain gauge patches at the rock sample and the Viton-rubber jacket.

Once the strain gauges were glued to the rock sample and the Viton rubber jacked was punctured, the jacked was imposed over the rock sample. Standard instant adhesive was used to glue the acoustic emission transducers to the rock sample. Acoustic emission transducers and wire feed troughs were sealed off by two layers of two-component adhesive (Loctite, Hysol).
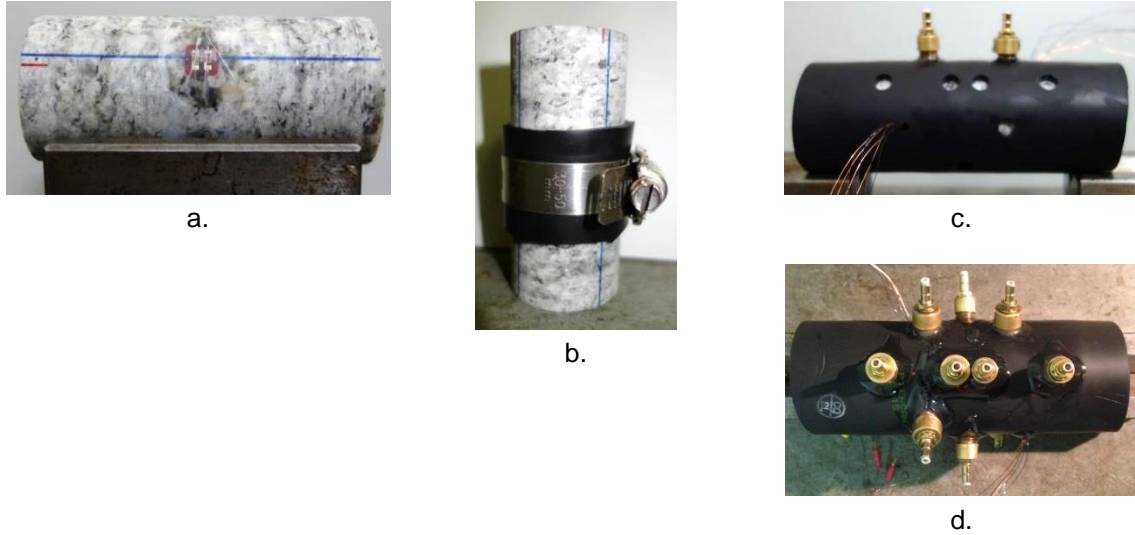
Figure 3.5: Progress of sample preparation: (a) Strain gauge patches attached to the center of the sample, 90° apart from each other, (b) Strain gauge patch fixation during dry time of glue, (c) Viton jacked imposed, wires of stain gauges laid, (d) acoustic emission transducers and wire feed troughs sealed off by two component adhesive.

3.1.3. Unconfined hydro-fracturing experiments

Samples for HF1 and HF2 were lathed to ensure parallelism. A new steel holder was manufactured for the larger sample diameter ($\emptyset\ 63.4\ x\ 126\ mm$). For both samples two $8\ mm$ boreholes, an injection and a production borehole, were drilled $25\ mm$ apart from each other using a core drill bit. Sample HF1 was equipped with four strain gauges patches (HBM, 1-XY93-6/120) glued 90° apart from each other using instant adhesive (ergo, 5011 Universal). The pins of the strain gauges were extended using insulated wire (HBM, 6 x LiY 0.14). For both samples HF1 and HF2 transducer 2 to 7 were evenly distributed around the injection borehole ensuring an even distribution of sensors. Sensor 1, which was placed closer to the injection borehole, was used as trigger sensor. For measuring global radial strain an extensometer (manufacturer: walter+bai ag, type: custom) was placed around the center of the rock sample (Figure 3.6, Figure 3.7).
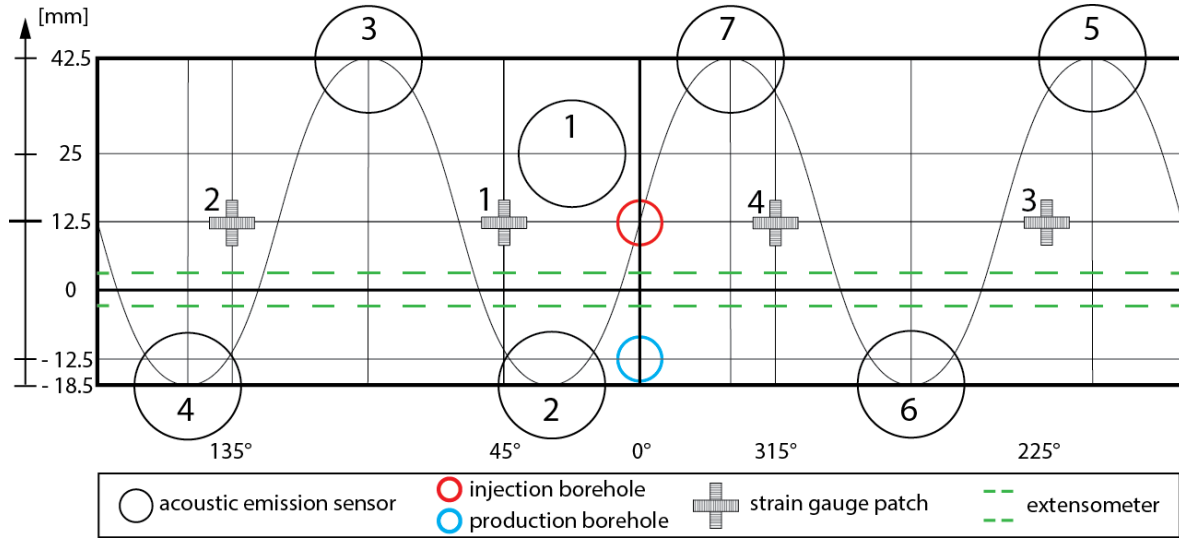
Figure 3.6: Arrangement of sensor position, injection boreholes, strain gauges patches and extensometer.
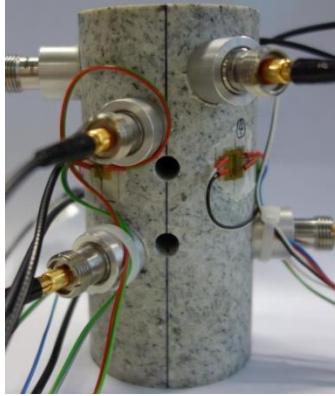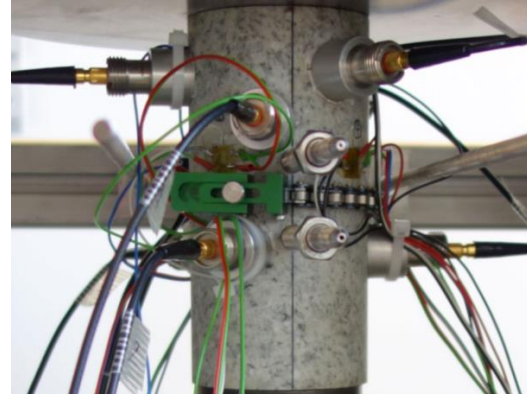
a.   b.

Figure 3.7: Sample for experiment HF1: a. AE sensors, strain gauges attached, injection boreholes drilled. b. Sample clamped in testing apparatus, extensometer and injection nozzles attached.

3.2. Experimental setups

3.2.1. Confined compression experiments

The cell used for the performed experiments is a triaxial oil medium loading cell ($\sigma_1 > \sigma_2 = \sigma_3$) manufactured by Sanchez Technologies. The apparatus was built in 2007. The confining pressure up to 100 MPa was directly applied to the rock sample by oil over a volumetric servo pump (Pump I), whereby the rock sample under investigation was protected by a Viton-rubber jacket against oil contamination (Figure 3.5, Figure 3.8).

Axial stress onto the rock sample was applied by an axial piston which was powered by a servopump (Pump II). The magnitude of the applied axial stress to the sample was estimated from the pressure measured by a transducer placed at the pressurised piston chamber and the

surface area of the rock sample. Investigating a cylindrical rock sample of 40 mm diameter allows a maximal axial stress of 680 MPa (Passelègue, 2014).

An important point to mention here is that this apparatus is not equipped with a balancing piston. Thus, any variation in confining pressure results in a variation of the applied axial force. An increasing confining pressure counteracts the introduced axial force by the cylinder and vice versa.
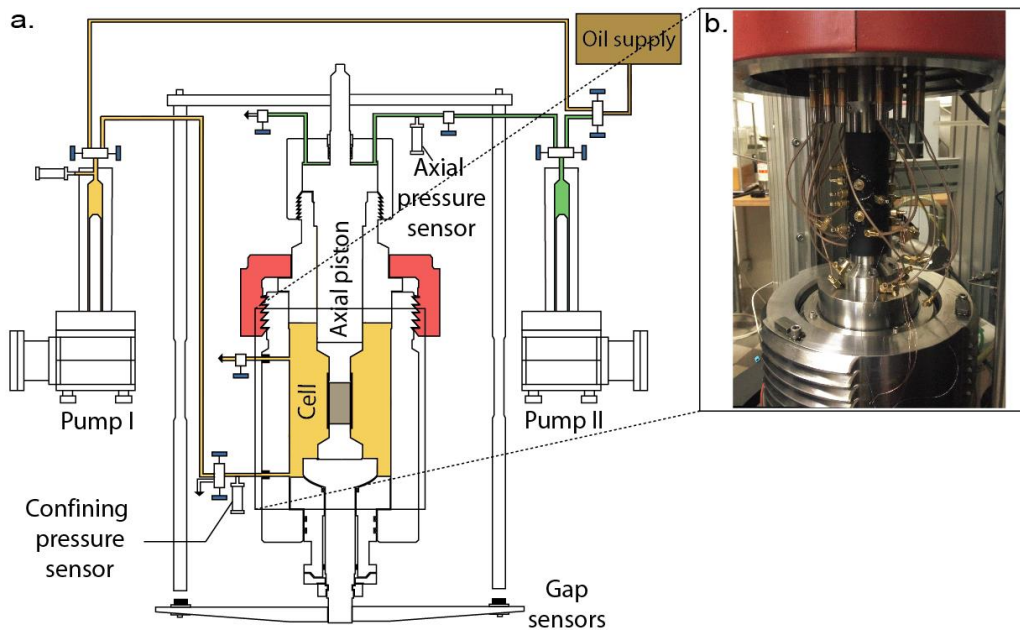
Figure 3.8: The experimental apparatus in detail: (a) Schematic drawing of the apparatus, (b) Inserted sample (modified after: Passelègue (2014)).

Like most triaxial apparatus, the triaxial cell manufactured by Sanchez Technologies, allows measuring the axial stress applied to the sample, as well as the axial displacement. The global axial displacement is measured outside the pressurised cell. It has to be noted that the measured axial displacement includes the elastic response of the components to which the sensors are attached, i.e. the sample assembly and the column of the apparatus. The advantage of the values measured externally is that they represent the global behaviour of the system during the entire experiment. In other words, also in destructive experiments, where internally placed sensors (strain gauges) are possibly destroyed, external measurements provide axial displacement data over the whole experiment.

The externally measured axial displacement was recorded and averaged by three gap sensors (Figure 3.8). The resolution of the measurement was about $0.1\,\mu m$ and the sampling rate was $100\,Hz$. Conducting a triaxial compression test, the gap sensors recorded the axial deformation of the rock sample under investigation, as well as the deformation of the apparatus over the entire experiment.

Axial and confining pressure were measured by two pressure sensors having a resolution of $10^{-3} MPa$. The sensor for the axial pressure was located close to the pressurised piston chamber, whereas the pressure sensor for the confining pressure was placed close to the cell. Data was read from the sensors at a sampling rate of $100\ Hz$. Pressure (axial stress) evolution was controlled by the software Falcon, which allowed a resolution up to $10^{-2} MPa$ (Passelègue, 2014).

While the gap sensors provided a good estimate of the axial displacement during the whole experiment, strain gauges glued directly onto the rock sample allowed the measurement of displacement locally. One strain gauge patch consists of two strain gauges which are orientated perpendicular to each other, allowing the measurement of axial and radial strains. Four patches were glued to the rock sample, whereas the four recorded strain values were averaged to an axial, ε_{ax}, and radial, ε_{rad}, strain. Strains were recorded at a sampling rate of $20\ Hz$. Volumetric strain, ε_{vol}, can be calculated as follows:

$$\varepsilon_{vol} = (1 + \varepsilon_{rad})^2 \cdot (1 + \varepsilon_{ax}) - 1 \qquad (6)$$

During the elastic part of a compression test, strain gauges provided an accurate estimate of occurring strains. As soon as microcracks began to form and to coalesce inside the rock sample the joint between strain gauge patch and rock surface began to weaken and accurate measurements were no longer possible. However, the internally measured axial strain in the elastic part of deformation was used to correct the external measured displacement from the influence of the stiffness of the apparatus using the following relation:

$$\varepsilon_{ax}^{gap} = \varepsilon_{ax}^{gaug} + \frac{\Delta\sigma}{E_{ap}} \qquad (7)$$

Where ε_{ax}^{gap} represents the average axial displacement measured by the gap sensors, ε_{ax}^{gaug} is the average axial strain measured by the four strain gauges, $\Delta\sigma$ is the applied differential stress and E_{ap} is the rigidity of the apparatus. The rigidity of the apparatus was estimated comparing the internal measured strain to the corrected external measured strain recorded during the elastic part of rock deformation. The value of the rigidity depends on the applied load, in the case of "Grimsel" granite, the rigidity ranges between 45 and $55\ GPa$ (Passelègue, 2014).

A piston pump was used to increase pore pressure (Quizix QX-1500). The pump pressure was limited to $10.3\ MPa$. The pore fluid was injected through openings located at the axial piston.

3.2.2. Unconfined hydro-fracturing experiments

An axial force was introduced by an axial compression cell (manufacturer: walter+bai ag, type: D-2000 C46H2). During an ongoing experiment the axial force introduced to the sample, the piston movement as well as the global radial strain were recorded at a sampling rate of $0.2\ Hz$. A strain gauge bridge amplifier (HBM, QuantumX MX1615B) was used to read out the quarter bridge strain gauges at a sampling rate of 10 Hz.

The injection nozzle ($\emptyset\ 7.8\ mm$) was sealed off by three O-rings ($2\ x\ 4\ mm$). The nozzle was inserted to a depth of $16\ mm$. The introduced thrust to the nozzle by an increased injection pressure was levelled out by an arrangement of rods (Figure 3.9).
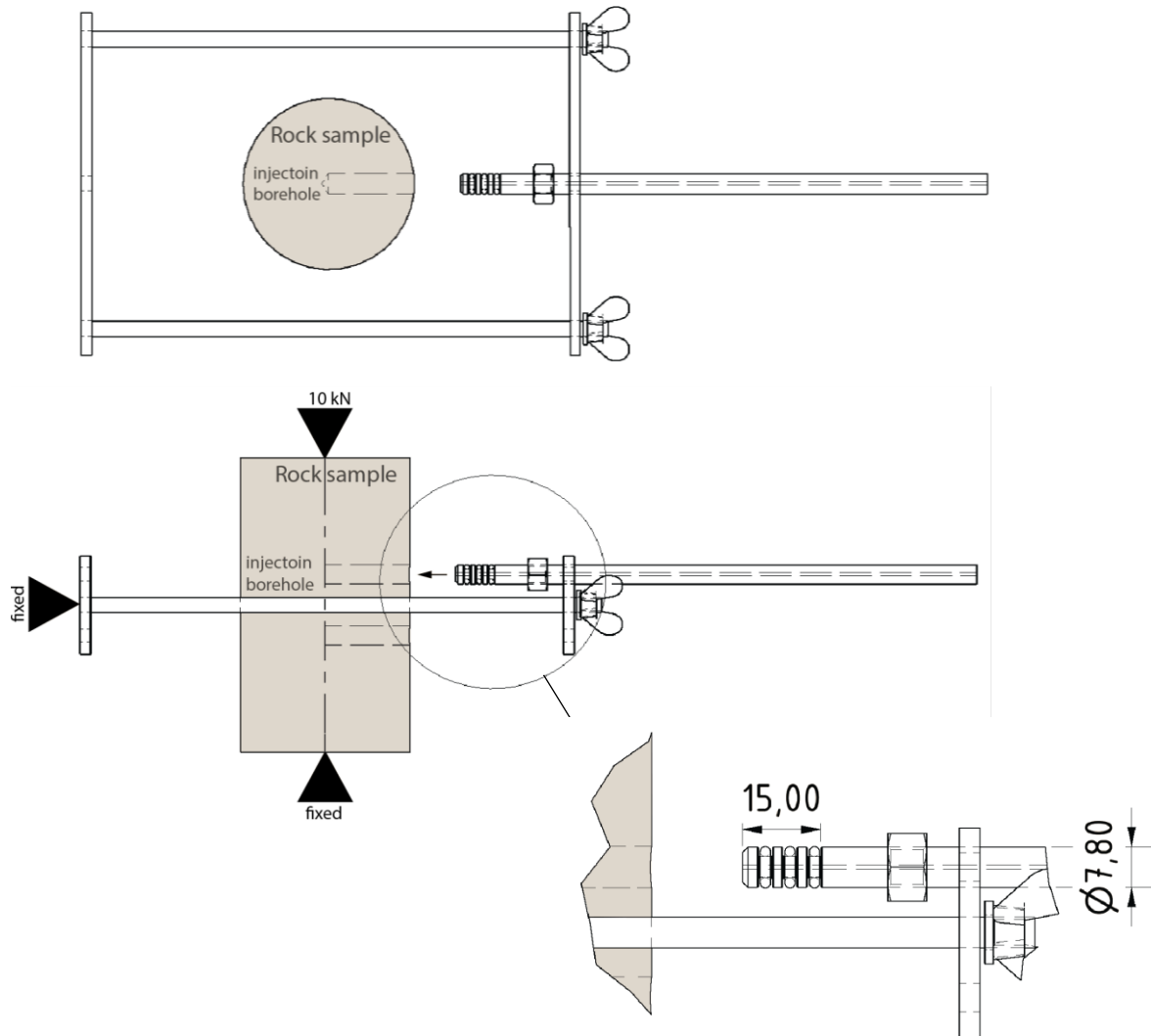
Figure 3.9: Setup for injection experiments: The arrangement of rods avoids the nozzle slipping out of the borehole.

The arrangement of rods was retained at the press assembly. Thus, the rock sample experienced no significant external forces other than in axial direction.

To apply injection pressure a syringe pump (ISCO Teledyne, model 2600, range: $0 - 500\ bar$) was used. Pump pressure (accuracy: $100\ kPa$), volume flow (accuracy: $0.001\ ml/min$) and injected volume (accuracy: $0.001\ ml$) were read out at a sampling rate of $1\ Hz$. The injection fluid was tap water at a temperature of $20\ °C$.

3.3. Acoustic emission monitoring system

To be able to capture and further investigate transient acoustic emission released during failure processes in rock, a well-chosen measurement chain as well as an appropriate acquisition system is needed. The term measurement chain includes all parts which deal with the analogues form of the measured signal, whereby the acquisition system represent the part which converts the analogues signal into a digital signal, further processes the signal, as well as records the signal.

The sensors represent the core of the measurement chain. When measuring acoustic emissions, piezo-electric sensors are normally used. The sensors respond directly to a displacement triggered by an elastic wave. Each sensor disposes of its own transfer function. The transfer function represents the way a sensor influences the output signal compared to its input signal. The output signal can be influenced through the sensor in terms of frequency, amplitude and phasing. The sensitive frequency range of the sensor needs to be in the frequency range of the expected signal to measure. A so called "flat" response over the frequency range of interest is desired. Speaking in terms of amplitude this means the amplification between output and sensor input signal is constant within the frequency range of interest. During the process of failure in granitic rock on a laboratory scale, elastic waves in the frequency range of 50 to 300 kHz are released. As an example the calibration procedure of the Glaser-type sensors used for the unconfined hydro-fracturing experiments reveals an almost constant amplification over the desired frequency range (Figure 3.10).
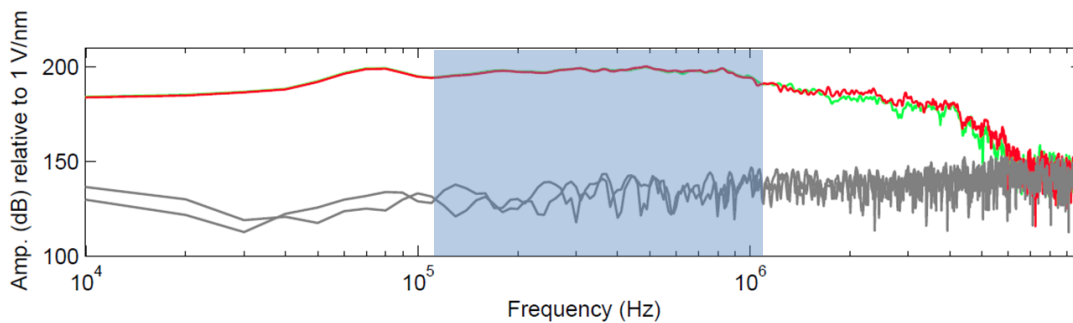
Figure 3.10: Amplification, frequency dependent, of a Glaser type sensor during glass capillary breakage on a steel plate. Green, Red are spectral sensor responses of two independent glass capillary fracture tests, Grey represents the noise estimation, light blue represents the frequency range of interest. (modified after: Services (2011))

Apart from the Glaser-type sensors, piezo-electric sensors are normally not calibrated. The transducers used for the confined experiments were custom made and have their sensitivity in the range of 10 to 500 kHz. For further waveform analysis it is assumed that sensors used within one experiment show the same response.

AE data acquisition systems are characterized by their method of data recording. Continuous data acquisition systems dispose of high data rate communication between sensors and data storage device, which allows the acquisition of continuous waveforms. Triggered data acquisition systems acquire data after a set threshold value is exceeded by the measured signal. The trigger criteria can be reached by only one channel, and trigger the data acquisition of all channels, or the trigger threshold can be set to multiple channels, which means the data acquisition is triggered by a measured signal and reached threshold on every single channel. The detection and counting of events of continuous acquired waveforms is done in post-processing. If a recorded signal exceeds the set threshold it is counted as an event. Triggered data acquisition systems detect, count and acquire AE events right away.

Comparing continuous and triggered data acquisition systems leads to one main downside of trigger based acquisition systems. After recognizing an event, the system stores the resulting data to the storage device which leads to an idle time which in turn puts event detection on hold. This means high frequent occurring events cannot be detected by trigger based acquisition systems. On the other hand, triggered data acquisition systems allow live monitoring of events during an experiment. Therefore, state of the art in laboratories is the combination of the two acquisition systems.

Furthermore, the acoustic emission monitoring system used for the confined experiments allows the measurement of average P-wave velocities between ray paths of all sensors.

3.3.1.   Confined compression experiments

Confined experiments where performed under triaxial conditions which require pressure resistant transducers.

Measurement chain

Generally, it has to be mentioned that the introduced pressure resistant transducers can either be used in receiving mode or in pulsing mode. 16 piezo-ceramic transducers are used to translate displacement into a measurable analogues voltage signal. A transducer consists of a lead-zirconate-titanate crystal, also known as PZT crystal (PI ceramic Pi255). The crystal has a diameter of 5 mm, a thickness of 0.5 mm and is encapsulated in a bras housing. The bras housing (outer diameter 7 mm) features a curve shaped front surface (curvature 40 mm), which corresponds to the cylinder curvature. The piezoelectric crystals are all polarised in the same direction and record preferably compressional waves. The transient, analogues signal is then relayed outside the pressurised cell by a coaxial cable (impedance 50 Ohm) where it is amplified at 45 dB (x177) by a Pulser Amplifier Desktop (PAD) unit (Passelègue, 2014).

Acquisition system

The amplified analogue signals during the confined experiments were digitalized and recorded by a Richter acquisition system. Four units are connected in Master and Slave mode housing 16 channels having a 16 bit analogue/digital resolution. The acquisition system was used in triggered mode. A trigger-hit-count (THC) unit allowed triggering of events on all 16 channels (Consultants, 2014b). Each time data acquisition was triggered, 1024 samples were recorded at a sampling rate of 10 MHz resulting in a recording time of about 102.4 us per event. In addition, a Pulser Interface Unit (PIU) was used to pulse each channel while the other channels record the initiated elastic wave. The initiated pulse consists of a high-frequent, 200 V pulse. Because of the known initiation time of the pulse, the known arrival time of the P-wave at each transducer and the known location of each transducer, average P-wave velocities between transducers along each ray path can be calculated.
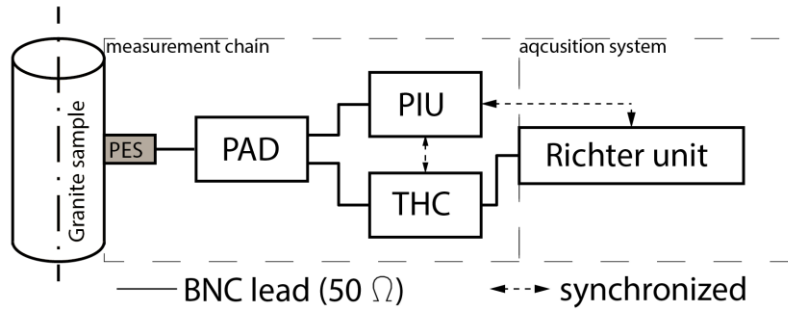
Figure 3.11: Acoustic emission monitoring system for the confined experiments. (PES: Piezo-Electric Sensor, PAD: Pulser Amplifier Desktop unit, PIU: Pulser Interface Unit, THC: Trigger Hit Count)

3.3.2. Unconfined hydro-fracturing experiments

Unconfined experiments under uniaxial loading where conducted using absolutely calibrated, non-pressure resistant point contact sensors (Glaser type). Note also, the acquisition system at ETH Zurich consists of two different systems. For the unconfined hydro-fracturing experiments two measurement systems (Richter, Cecchi) providing four channels each were used in combination. To trigger data recording of both systems at once, the signal of one sensor was split.

Measurement chain

Seven Glaser sensors (SteveCo KRNBB-PC) were used here. The Glaser sensors have a cone shaped single tip, which protrudes the stain less steel casing of the sensor and allows a point contact to the rock sample. Furthermore, the sensors are absolutely calibrated. Calibration is performed comparing the measured response of a glass capillary (0.4 mm) breakage on a steel plate (50.8 mm) to a theoretical calculated displacement assuming the capillary breakage represents a step function. Calibration shows a flat response in a range of 50 kHz to 1 MHz. Over a frequency range of 20 kHz to 1 MHz the sensors show a sensitivity of 15 mV/nm $\pm$ 4 dB (McLaskey et al., 2012; Services, 2011).

The sensor itself includes a JFET (junction field-effect transistor) pre-amplifier. Then, a 50 Ohm impedance coaxial cable connects the sensors to the main amplifier (AMP-12BB-J). The chosen calibration mode (Cal Mode) amplifies the signal by -0.92 dB (x 0.9) and limits the output voltage to 4 Volts (Services, 2011).

Acquisition system

For experiment HF1 and HF2 the two acquisition systems at ETH Zurich were used in combination. Four channels were provided by a Richter data acquisition unit (same type as for the confined compression experiments). Another four channels were provided by a Cecchi acquisition unit, providing a sampling rate of 10 MHz and an analogue/digital resolution of 12 bit. 1024 samples were recorded when an event exceeded the set threshold.

One sensor is used for triggering purposes and is connected to a Pulser Amplifier Desktop unit (PAD), which amplifies the signal at 30 dB. Additionally, the PAD allows a splitting of the signal, which is needed to trigger the two different acquisition systems at once. The Pulser Interface Unit (PIU) is used to supply the PAD.
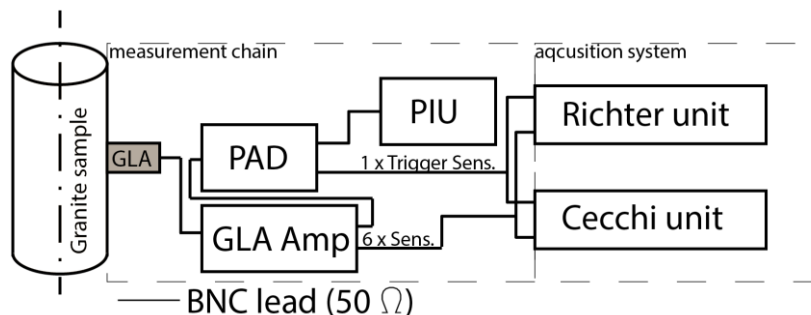

Figure 3.12: Acoustic emission monitoring system used for HF1 and HF2. One sensor triggers both acquisition units. (GLA: Glaser-type sensors, PAD: Pulser Amplifier Desktop unit, PIU: Pulser Interface Unit)

3.4. Data analysis

Acoustic emission recorded were analysed using the commercial software InSite, where picking algorithms as well as event localization algorithms are included. The advantage of InSite is that the software is comparably user-friendly and contains all tools required for event localization. This section highlights elements found in Consultants (2014a, 2015).

3.4.1.   Localization Algorithm

For localizing AE a collapsing grid search algorithm was used. The algorithm allows the implantation of a time dependent transversely-isotropic velocity model. The following main steps are followed by the algorithm:

1. A single velocity is calculated for a ray path between a possible event location P and the transducer R.
2. The ray path between P and R is calculated as three dimensional vector (azimuth, plunge, and length).
3. The velocity for the ray path is calculated depending on the implemented velocity model.

The algorithm searches a three dimensional regularly spaced grid for the minimum misfit between measured travel times (picked P-wave onsets) at each transducer and theoretical travel times calculated between the possible event location and the transducers. An initial coarse grid is first searched for the minimum misfit position. It is then assumed that this minimum is spatially close to the global minimum and generates a smaller and finer grid around this position. This process continues until a specified resolution is met.

The following settings were used during this work:

Table 3.1: Settings collapsing grid search algorithm

Grid limit: (north, east, depth)	-35, 35; -35, 35; -50, 50 mm
Cell dimension (initial grid):	2 mm
Desired resolution:	0.1 mm
Collapsing buffer:	4

The collapsing buffer represents the half-width in uncollapsed cells of the new grid.

3.4.2.   Seismic P-wave velocity model

For calculating theoretical arrival times of possible event location a model is needed describing the velocity distribution inside the 3D search space. A time-dependent homogeneous-isotropic velocity model (Hi-model) additionally to a time-dependent transversely-isotropic velocity model (Ti-model) was developed for the confined experiments. The Hi-model assumes no velocity variation with position (homogeneous) and no velocity variation with direction (isotropic). The Ti-model assumes varying velocities depending on ray path orientation through the search space with respect to an axis of symmetry defined by a vector.

The raypath velocity V_r is given as follows:

$$V_r = \left(\frac{V_{||} + V_{\perp}}{2}\right) - \left(\frac{V_{||} + V_{\perp}}{2}\right) cos(\pi - 2\theta) \tag{8}$$

Where $V_{||}$ represents the axial velocity, $V_{\perp}$ the velocity perpendicular to the cylinder axis and θ the angle between the raypath and the axis of symmetry.

The anisotropy factor is defined by:

$$V_{\perp} = \alpha \cdot V_{||} \tag{9}$$

For the confined experiments, seismic P-wave velocities were modeled depending on obtained arrival times of initiated survey shots. During a survey each single transducer in an array is actuated and emits an elastic wave (shot), while the other sensors act as receivers. Travel times between transducers are then obtained by picking P-wave onsets of recorded shots. Assuming a direct ray path between transducers average velocities between transducers are calculated.

For the Ti-model the cylinder axis represents the axis of symmetry, implying a high velocity in axial and a slow velocity in radial direction. Velocities of inclined raypath are calculated according to equation 8.

3.4.3. P-wave picking

Manual P-wave picking can be a more accurate technique of detecting onsets of elastic compressional waves compared to the onset detection by automatic picking algorithms. It includes a subjective component but if the same person picks all events it is seen as consistent.

As soon as a high number of events are recorded manual picking is too time consuming and automatic picking algorithms are used. During this work the RMS auto-picking algorithm was implemented. The algorithm calculates an auto-picking function, F_i, using a moving window approach. At each data point, i, of a waveform a front window and a back window is generated according to equation 10.

$$F_i = \frac{\sum_{j=i+1}^{i+FW} A_j^2}{\sum_{j=i-1}^{i-BW} A_j^2} \tag{10}$$

Where A_i is the amplitude at point i, FW is the length of the Front-window in data points and BW in the length of the Back-window in data points. The value of the auto-picking function represents the relative energy contained in the front window compared to the back window. Peaks occur where waveforms suddenly increase.

The following settings were used here:

Table 3.2: Settings autopick function

Back-window length:	60 samples
Front-window length:	15 samples
Picking Threshold:	15 samples

The settings used are rather conservative, which results in consideration of only strong P-wave onsets which clearly differ from the noise level. On one hand, this improves the accuracy of picked events. On the other hand, events which feature weak onsets are not considered which could in turn lead to an incomplete event catalogue.

3.4.4. Determination of magnitudes

Confined compression experiment

To successfully located events a relative location magnitude, M_{Loc}, is calculated as follows:

$$M_{Loc} = log\left(\frac{\sum_{m=1}^{m=N}\left(W_{RMS_m} \cdot d_m\right)}{N}\right) \tag{11}$$

Where W_{RMSm} is the peak RMS (root mean square) amplitude at each transducer, m, used for localization. d_m is the ray path length between event location and transducer location. N represents the total number of transducers used for localization.

Unconfined hydrofracture experiment

For the unconfined hydrofracture experiment magnitudes were calculated according to Goebel et al. (2012), using the peak amplitude recorded at the trigger sensor. At first, the peak amplitude was corrected for geometrical spreading on a 10 mm reference sphere assuming elastically propagating, spherical waves of a point source:

$$A = \sqrt{\left(\frac{r_i}{10} A_{max}\right)} \tag{12}$$

where A_{max} is the recorded peak amplitude at the trigger sensor and r_i is the distance between event location and sensor. A magnitude was then assigned to each recorded event with the simple equation:

$$M = \log(A) \tag{13}$$

3.4.5.　　Magnitude of completeness (Mc)

Mc is calculated using the Goodness-of-Fit test (GFT) according to Wiemer et al. (2000) assuming a Gutenberg-Richter (GR) power law distribution of magnitudes. The difference between a synthetic frequency-magnate distribution (FMD) following the GR power law perfectly and the observed FMD is calculated. The goodness of fit, G, is estimated by computing the absolute difference between the number of events in each magnitude bin of the synthetic FMD and to the observed FMD. In equation 12, B_i represents the observed and S_i the predicted cumulative number of events in each bin, whereas G is given in percentage normalized by the total number of observed events $\sum_i B_i$.

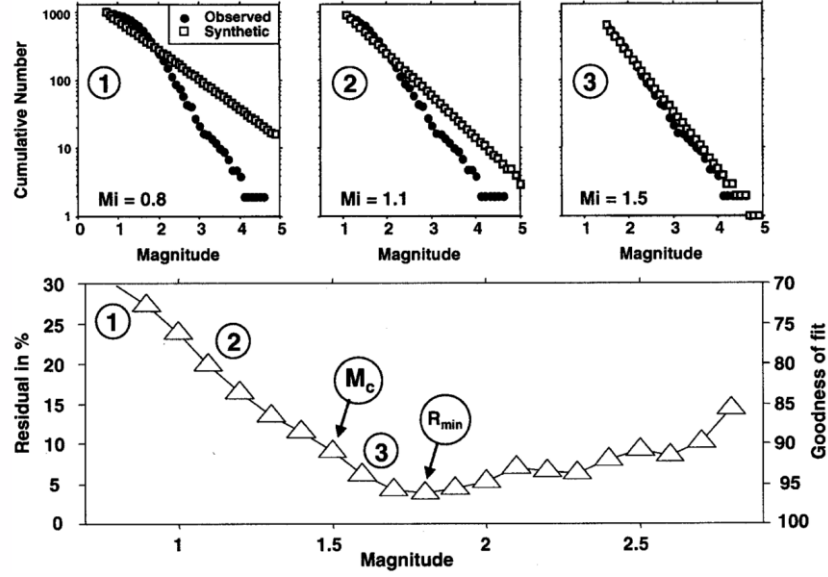$$G = 100 - \left(\frac{\sum_{M_i}^{M_{max}} |B_i - S_i|}{\sum_i B_i}\right) \cdot 100 \tag{14}$$

Figure 3.13: Explanation of GFT to obtain Mc. The three top figures show synthetic fits to an observed catalogue at different magnitude cutoffs. The bottom figure shows the goodness of fit, G, in percentage of the differences between observed and synthetic FMD as a function of magnitude cut-off. Mc is selected at which 90 % of the observed data is modeled by the synthetic FMD. (modified after: Wiemer et al. (2000))

3.4.6.   Magnitude-frequency b-value

To estimate the b-value the maximum-likelihood technique according to Woessner (2005) was used:

$$b = \frac{log_{10}(e)}{\left[\langle M \rangle - (M_C - \frac{\Delta M_{bin}}{2})\right]} \tag{15}$$

b describes the relative size distribution of events, $\langle M \rangle$ is the mean magnitude of the event catalogue, M_C is the magnitude of completeness of the catalogue and ΔM_{bin} represents the bin width of the catalogue.

3.4.7.   Accuracy of localization

A velocity model representing the real velocity distribution as accurate as possible and an accurate picking of P-wave onsets are seen as having the biggest impact on an accurate localization. Errors of signal detection, signal transmission, location algorithms as well as miss located transducers are seen as having a minor impact on localization accuracy.

In this work absolute localization accuracies were estimated locating survey shots of transducers. Differences between located shot and transducer location were interpreted as absolute location accuracy given the assumption that transducer emit acoustic waves at an exact known position.

34

4. Results

4.1. Localization experiment in homogeneous-isotropic media

To gain first insights on localization procedures, two pencil-lead breakages (PLB) were located on the surface of an aluminum cylinder ($76\ mm$ in diameter and $80\ mm$ in length). PLB's were established as a standard AE source. Thereby, the lead tip of a mechanical pencil was pressed firmly against the specimen under investigation until the lead broke. The instantaneous break of the lead released the accumulated stress and the resulting microscopic displacement at the surface leads to an elastic wave, which propagates through the specimen (Sause, 2011). The emitted elastic wave is then detected by an array of four sensors. PLB's are strong events, easy to pick and distinguish themselves very much from the noise level of the sensor (Figure 4.1). The events were recorded continuously by a Richter acquisition system (Consultants, 2014b).

As reference localization, recorded waveforms were picked manually. A homogeneous-isotropic velocity model was implemented for localization, using a P-wave velocity of $6.375\ m/s$ (Olympus, 2015). Quantitative and qualitative influences on localization accuracy were investigated by introducing a miss pick by $\pm\ 0.5\ us$ ($\pm\ 5$ samples) on each sensor as well as by changing the seismic P-wave velocity by $\pm\ 5\ \%$.
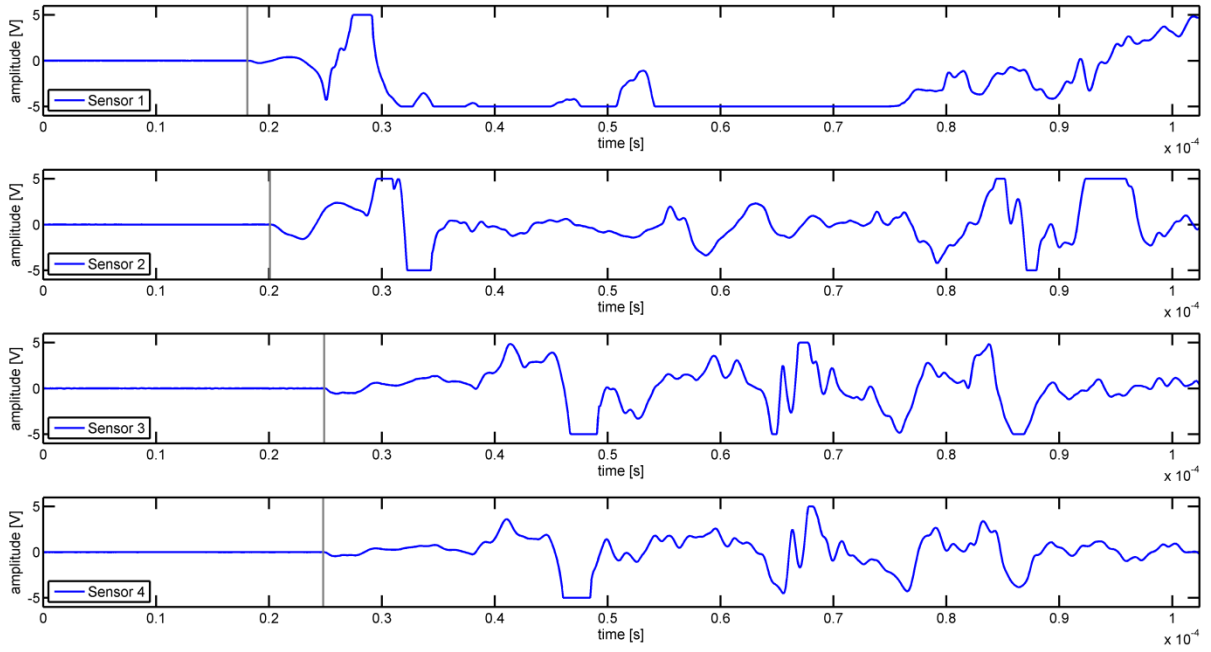
Figure 4.1: Waveforms of PLB 1 recorded over 102,4 us, first motion P-wave picked manually [grey vertical line].

Localizing the manually picked event results in an absolute localization accuracy of $0.2\ mm$ (distance between initiated and localized event) for PLB 1 and $2\ mm$ for PLB 2. Automatic picking produced an absolute localization accuracy of $4.8\ mm$ for PLB 1, resp. $10.1\ mm$ for PLB 2 (Figure 4.2, Figure 4.3).

Figure 4.2: Induced PLB's on the aluminum sample.

Figure 4.3: xy-, xz-view of localization results for manual picking, automatic picking, changing velocity models (reference: manual picks) and miss picks (reference: manual picks).
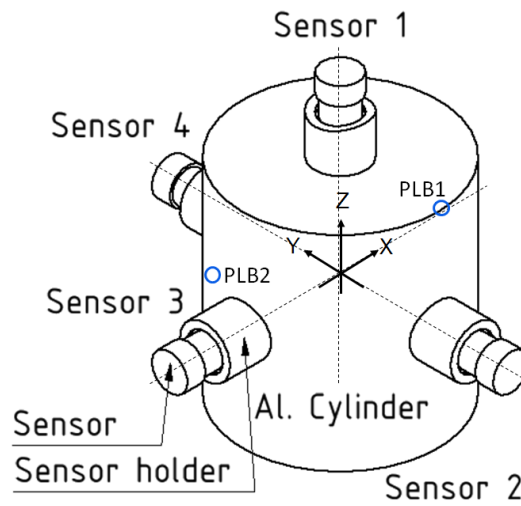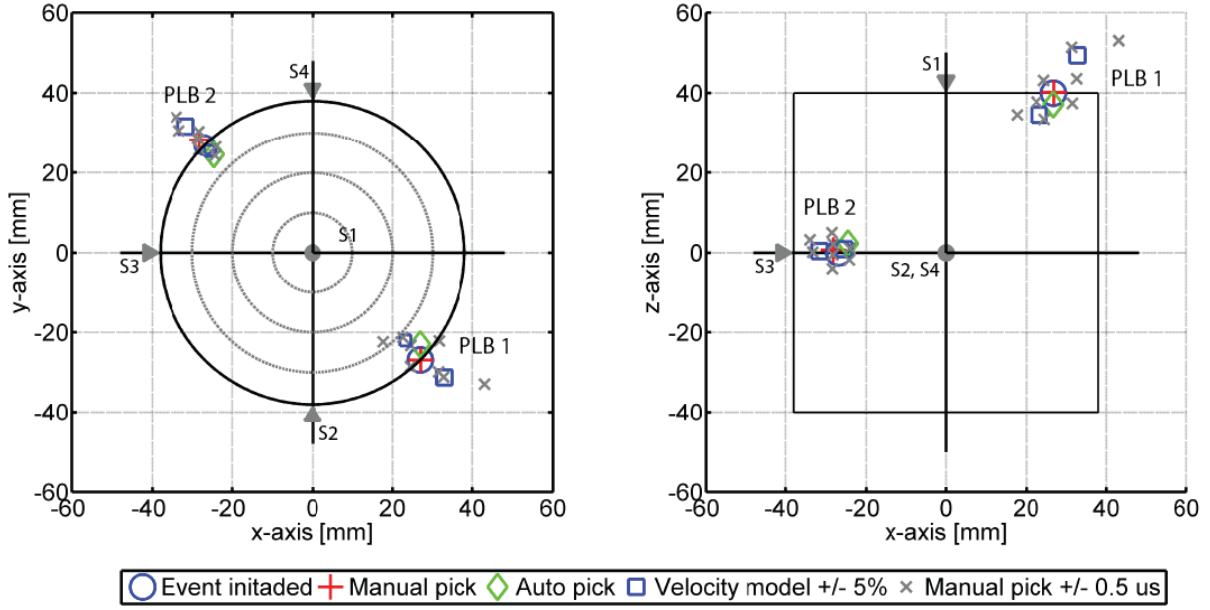
A lower P-wave velocity leads to localization closer to the center of the aluminum cylinder, whereas a higher velocity leads to localization of the event outside the cylinder. Identifying the influence of miss picks each channel has been modified separately, leading to 8 different events localization. Here, the same trend holds shorter travel times lead to localization closer to the center, whereas with longer travel times the events are localized outside the sample. Miss picking the waveform of sensor 3 of PLB 1 by $+0.5\,\mu s$ leads to a maximum deviation of $21.6\,mm$. Miss picking the waveform of sensor 2 of PLB 2 by $+0.5\,\mu s$ leads to a maximum deviation of $10.5\,mm$.

It can be concluded that, a small change in onset picks lead to a comparable large change in location because of the limited sensor array of only four sensors. Localizations outside the cylinder volume, i.e. outside the sensor array reveal a greater deviation from the point of PLB initiation than localizations inside the sensor array. These findings contribute to a feeling for influences on localization by different errors.

4.2. Confined compression experiment GR1

4.2.1.   Mechanical observation, event count

At $40\,MPa$ confining pressure GR1 was axially compressed at a constant rate of $2\,MPa\,min^{-1}$ until failure. Failure was detected at a differential stress of $263.2\,MPa$ after $6770\,s$. A total of 4150 events were counted during an experiment time of $9800\,s$. 2300

foreshocks are counted before failure. The very first AE was recorded after $2670\,s$ (Figure 4.4).
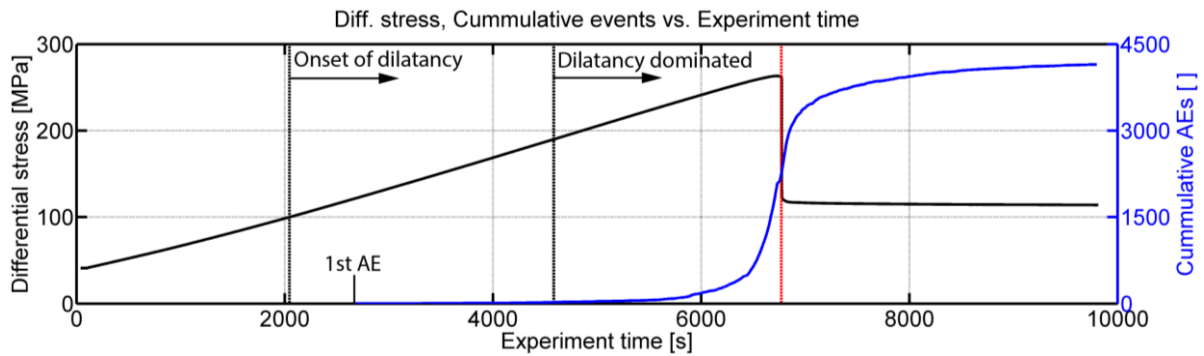

Figure 4.4: Overview of triaxial compression experiment GR1. Strain gauge measurements (Figure 4.5) suggest the onset of microcrack initiation after $2050\,s$. After $4600\,s$ microcracks begin to coalesce and form macroscopic fracture. A rapid increase of AE rate is detected after 75 % of peak stress is reached.

Volumetric strain deviates from linearity after $2050\,s$ which marks the onset of dilatancy. After $4600\,s$ peak volumetric strain was reached, which represents the transition between compaction dominated and dilatancy dominated deformation (Figure 4.5).

Recorded AE were not further analysed. Reasons were faulty coaxial cables fed through into the pressurised cell which limited the number of working transducers.
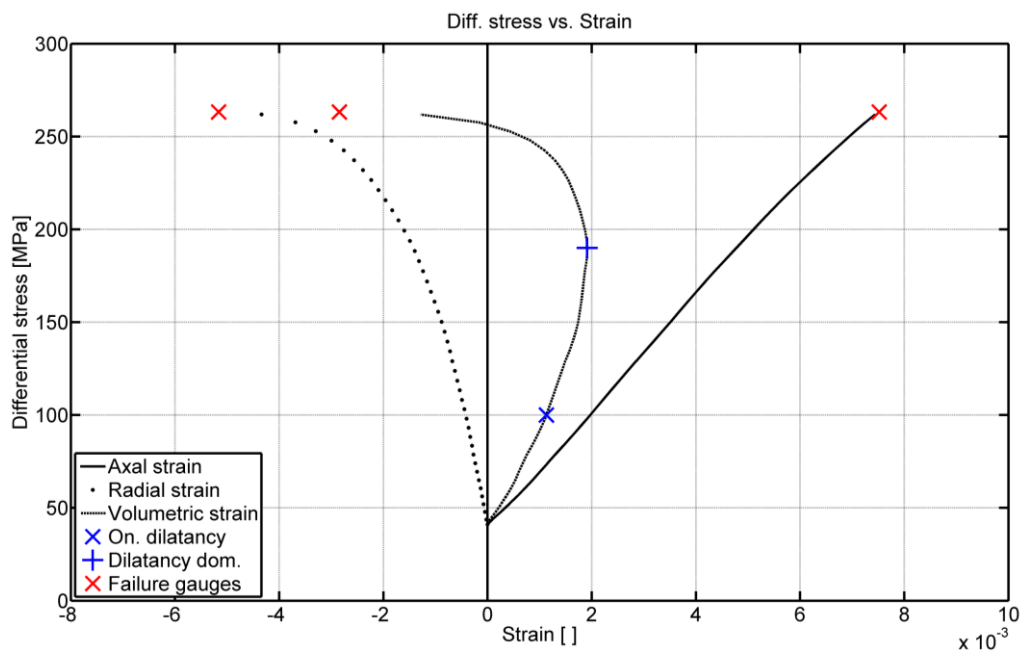

Figure 4.5: Axial-, radial- and volumetric strain vs. applied differential stress of GR1. Microcrack initiation (onset of dilatancy) and the onset of microcrack coalescence (dilatancy dominated regime) are estimated. Gauges fail at stress drop.

4.3. Confined compression experiment GR2

4.3.1.　　　Mechanical observation, event count

Under $40\,MPa$ confining pressure GR2 was axially preloaded at a constant rate of $4.7\,MPa\,min^{-1}$ to $238\,MPa$ (90 % of peak stress reached during experiment GR1). Pore fluid was injected at a constant pump pressure of $10\,MPa$. After an idle time of $1800\,s$ axial compression pressure was increased to $254\,MPa$ (97 % of peak stress reached during experiment GR1). After $900\,s$ axial compression pressure was increased further to $265.8\,MPa$. Idle time during period 3 lasted for $1300\,s$. Failure was detected after $7533\,s$ after the experiment has started. A total of 7000 events were counted during an experiment time of $10000\,s$. 5500 foreshocks are counted before failure. The very first AE was recorded after $1826\,s$ (Figure 4.6).
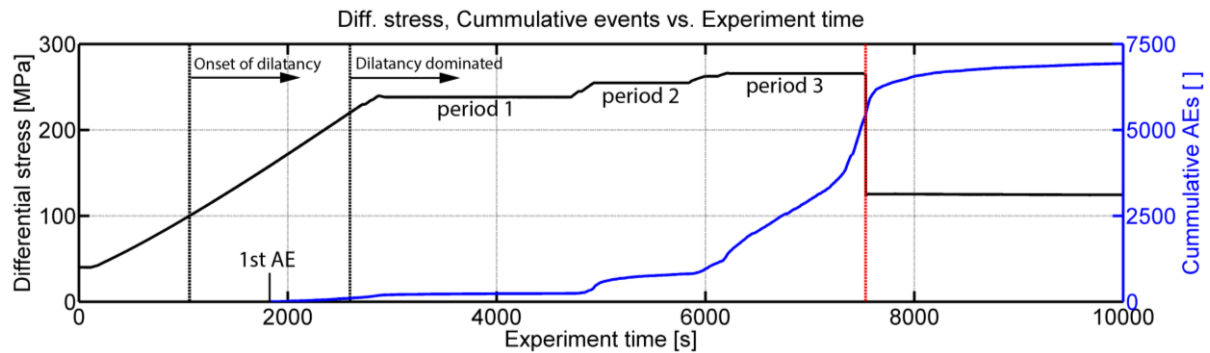

Figure 4.6: Overview of hydraulic shear experiment GR2. Measurements of strain gauges (Figure 4.7) suggest the onset of microcrack initiation after $1060\,s$. After $2600\,s$ microcracks begin to coalesce and form macroscopic fractures. During idle period 1, no microcracks are formed. Period 2 and period 3 reveals to be unstable, AE rate increases towards failure.
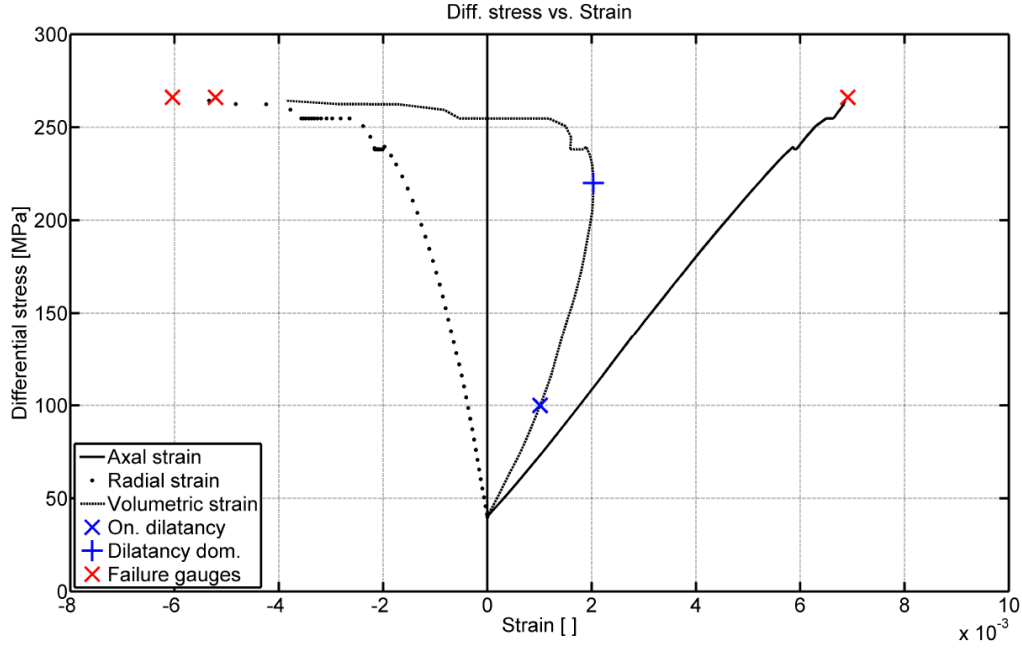
Figure 4.7: Axial-, radial- and volumetric strain vs. applied differential stress of GR2. Microcrack initiation (onset of dilatancy at $1060\,s$) and the onset of microcrack coalescence (dilatancy dominated regime at $2600\,s$) are estimated. Gauges fail at stress drop.

Figure 4.8 shows the applied pump pressure during the experiment. Visual observation after the experiment showed no diffusion of pore fluid injected through openings inside the axial piston into the granite sample. Only the surface of the front face was wetted by injection fluid. Therefore, it is suspected that the injected fluid had no influence on deformation of GR2.

Figure 4.8: Evolution of pump pressure during experiment GR2.

4.3.2. Implemented velocity models

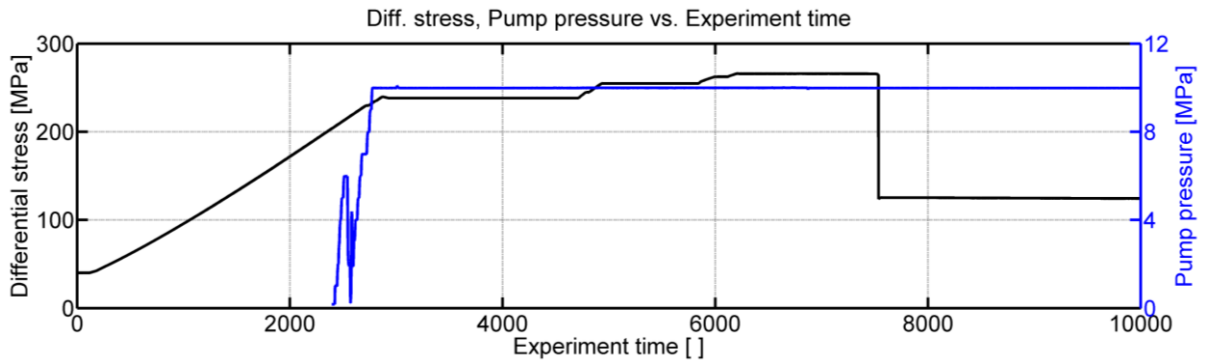Apparent P-wave velocities between transducer pairs were calculated based on surveys taken during the experiment (see also Section 3.4.2). Figure 4.9 shows calculated velocities for horizontal (0°) and inclined ray path ($31 - 90°$).
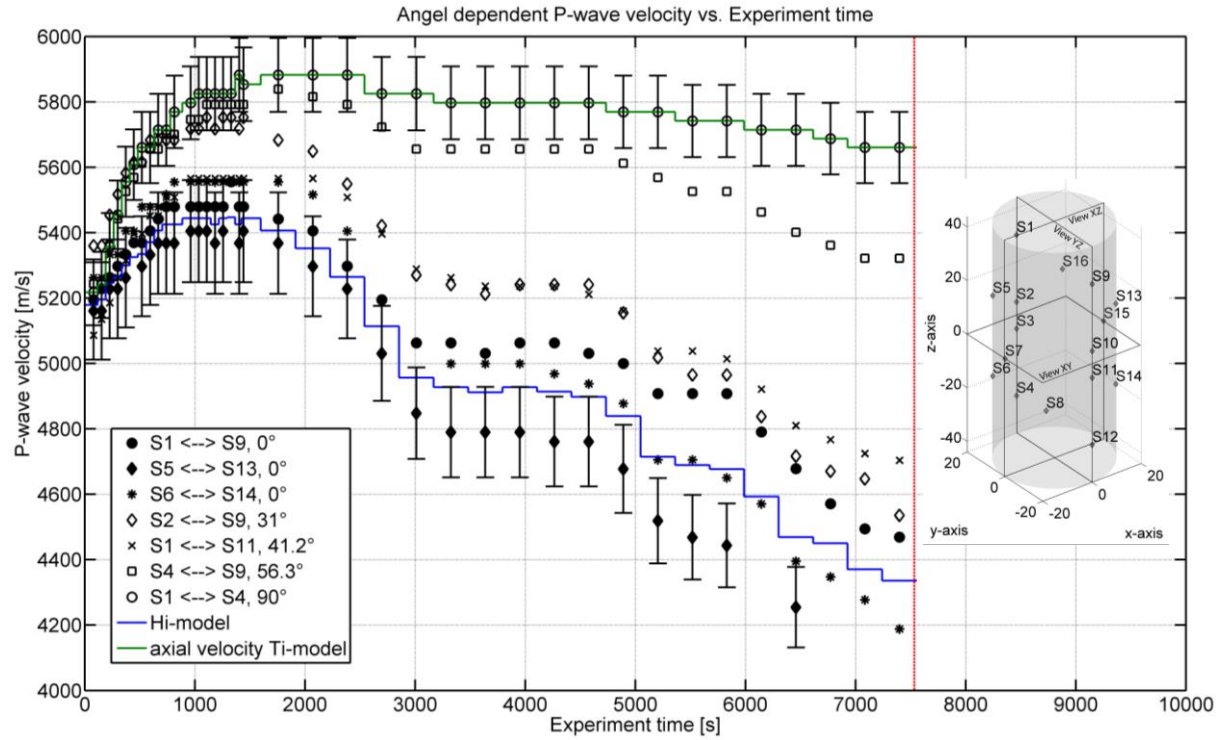

Figure 4.9: Horizontal (filled markers) and inclined P-wave velocities. Error bars, shown for the highest and lowest velocities, represent an estimated error assuming an error in sensor location of $\pm 2\,mm$ and an error in travel time picking of $\pm 0.2\,us$ ($\pm 2\,samples$). Measured travel times between each sensor pair were averaged. Velocity models were discretized in time according to surveys taken.

Horizontal and inclined P-wave velocities of the intact sample at the beginning of the experiment are in a range of $\pm 200\,m/s$. During compaction of the sample P-wave velocities increase. With increased crack density horizontal velocities decrease while inclined velocities show a lower dependency on forming microcracks.

For localization two velocity models were determined. The homogeneous-isotropic model (Hi-model, Figure 4.9) was calculated averaging the horizontal velocity over time obtained between sensor 1, 9 and sensor 5, 13. The transversely-isotropic model was calculated by determining the anisotropy factor (i.e. $V_{||}$ = velocity measured from sensor 1 to 9, $V_{\perp}$ = is represented by the Hi-model) according to Section 3.4.2.

4.3.3.   Localized AE, comparison to CT-scan

The 5 450 foreshocks were taken for further analysis. Using conservative automatic picking settings (Table 4.1), implementing the Ti-model, 2750 events were localized. Location algorithm settings are listed in Table 4.2. Figure 4.10 shows the localization result for the 2750 AE. Residual times (i.e. difference between measured arrival times and theoretical arrival times) exceeding the set threshold made the remaining events not locatable.

Table 4.1: Settings automatic picking algorithm

Method:	Picking threshold:	Back window length:	Front window length:
RMS amplitude	8 in AF	60 samples	15 samples

Table 4.2: Settings location algorithm

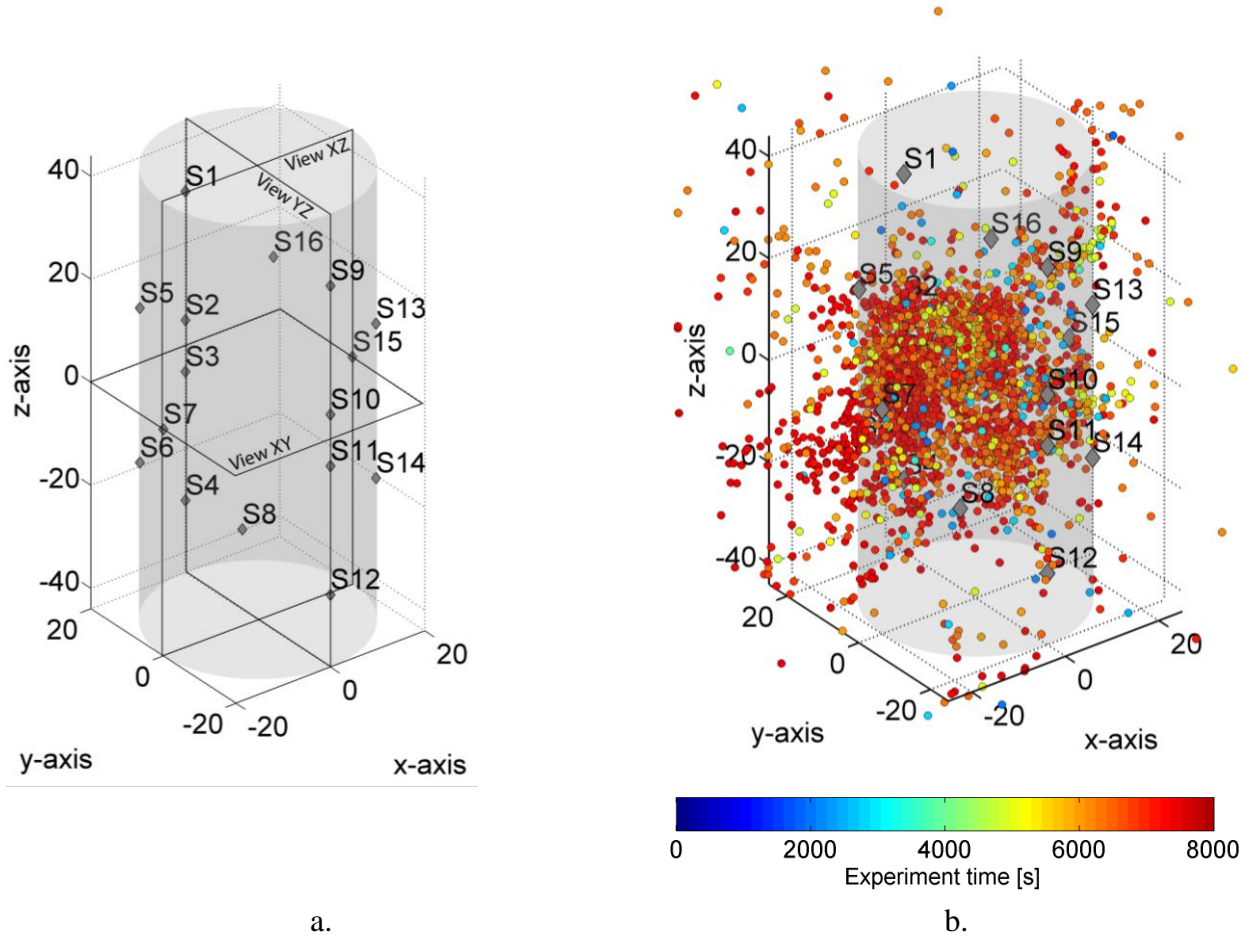| Localisation algorithm:	Min. P-wave arrivals:	Max. residuals:
Collapsing grid search	6	0.8 μs

a.

b.

Figure 4.10: (a) gives an overview of sensor position and views used for analyses purposes. (b) shows localization of the 2734 AE. Localized AE are colored according to the experiment time.

2000 of the 2750 events are localized inside the cylinder volume. The localization algorithm uses limited search space (x, y-axis: $\pm 35\ mm$, z-axis: $\pm 50\ mm$), this leads to a pile up of some events at search space boundaries, which would otherwise be localized further outside the cylinder.

Figure 4.12 shows localization results based on time sequences presented in Figure 4.11. Results are obtained implementing the time dependent homogeneous-isotropic velocity model (Hi-model), resp. the Ti-model. Sequence 1 shows microcracks preferably forming, almost equally distributed inside the sensor array. During idle time of sequence 2, only 20 AE (19 AE) are localized, one could estimate a clustering of events close to sensor 9. Increasing differential stress during sequence 3 leads to some clustering of events in the region of sensor 2, 3 and 15. XY-views have been taken for sequence 1 to 5 (Figure 4.13), which reveals the observed clustering during sequence 3 partially outside the cylinder using the Hi-model. Increasing load during sequence 4 leads to a confirmation of clustered events around sensor 2, 3 and 15. A macroscopic fracture can be estimated which started to nucleate during sequence 3. Sequence 4 represents no further energy applied by the axial piston, deformation becomes unstable and time dependent. However, in the $900\ s$ the rock sample is able to support the applied load and the AE-rate converges to zero. Increasing differential stress by $10\ MPa$ after sequence 4, leads to an increase in AE-rate. The crack coalescence threshold is met, microcrack formation and coalescence is time dependent and self-preserving. During sequence 4 and 5 number of events localized outside the cylinder increase drastically. Overall, AE density drops near the ends of the sample. Reason for this is the lower deviatoric stress caused by the lateral support of the steal end plugs (Lockner, 1993). Occurrences are no longer represented by the implemented Hi-model because of the increased microcrack density. The Ti-model on the other hand seems to represent the occurrences more accurate.
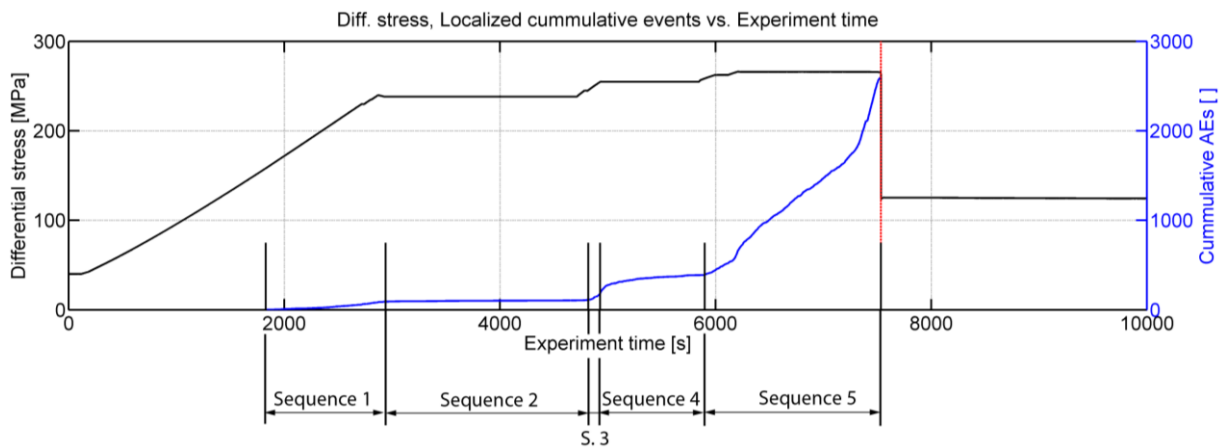

Figure 4.11: Sequenced experiment overview. The red vertical line represents failure of the rock sample.

Comparison to CT-scan images

CT-scan images were performed of the fractured sample. The scans were performed at the ETH Zurich by a phoenix v|tome|x s 240 X-ray scanner (GE Sensing & Inspection Technologies GmbH, Wunstorf, Germany). The acquisition parameters are shown in table:

Table 4.3: Acquisition parameter CT-scan

Scanning resolution:	Current:	Voltage:	number of images:	averaged images:
70.000 µm voxel edge length	140 µA	700 kV	1600	1 (skip: 0)
Filter:	**Binning:**	**Exposure time per image:**	**Scan duration:**	**Detector sensitivity:**
0.1 mm copper	2x2	250 milliseconds	10 minutes	2

For reconstruction (in 32 bit float format) no ring artifact correction, but an autoscanoptimization and a beam hardening correction was performed (beam hardening correction with a correction value of 4 assuming different materials). Reconstructed original images (32 bit float) were downscaled to unsigned 8-bit format for further data processing.

In Figure 4.14, subsets of AE taken at the position of the particular CT-scan images (volume of captured AE, $\pm 1.5\ mm$ normal to the CT-scan image plain) are compared to section views of the CT scan. It can be observed that the final fracture which led to failure was initiated in the region of sensor 2, 3 and 16 at $z = 0\ mm$. Also, the inclined macroscopic fracture shows a good agreement between AE and CT-scan. Figure 4.15 shows the increased microcrack density throughout the sample cross section.

Figure 4.12: YZ-View of localized events during sequence 1 to 5 according to Figure 4.11. The colored markers represent location of events additionally to the experiment time. Sensor positions are marked by grey diamond.
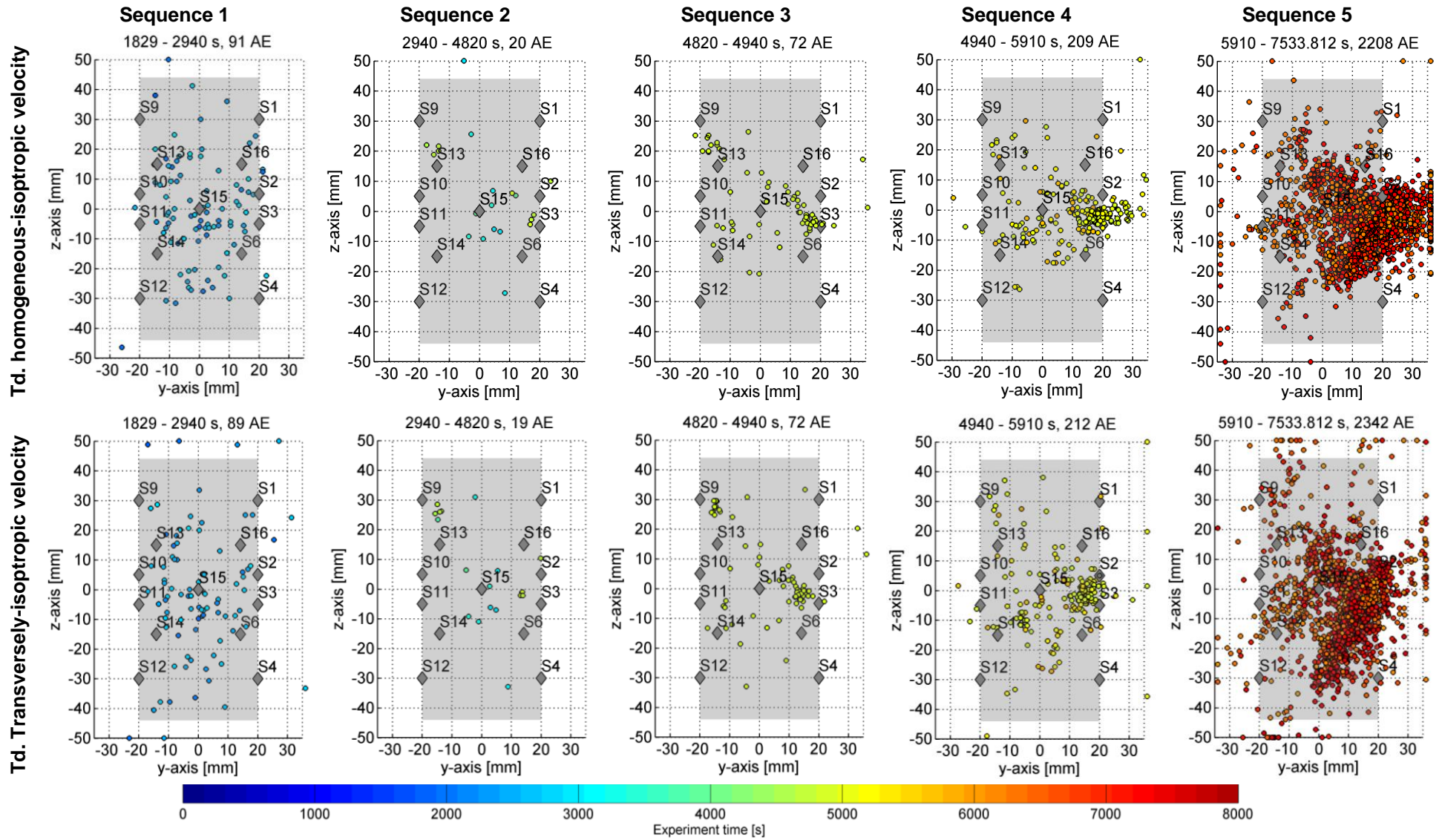
Figure 4.13: XY-View of localized events during sequence 1 to 5 according to Figure 4.11. . The colored markers represent location of events additionally to the experiment time. Sensor positions are marked by grey diamond.

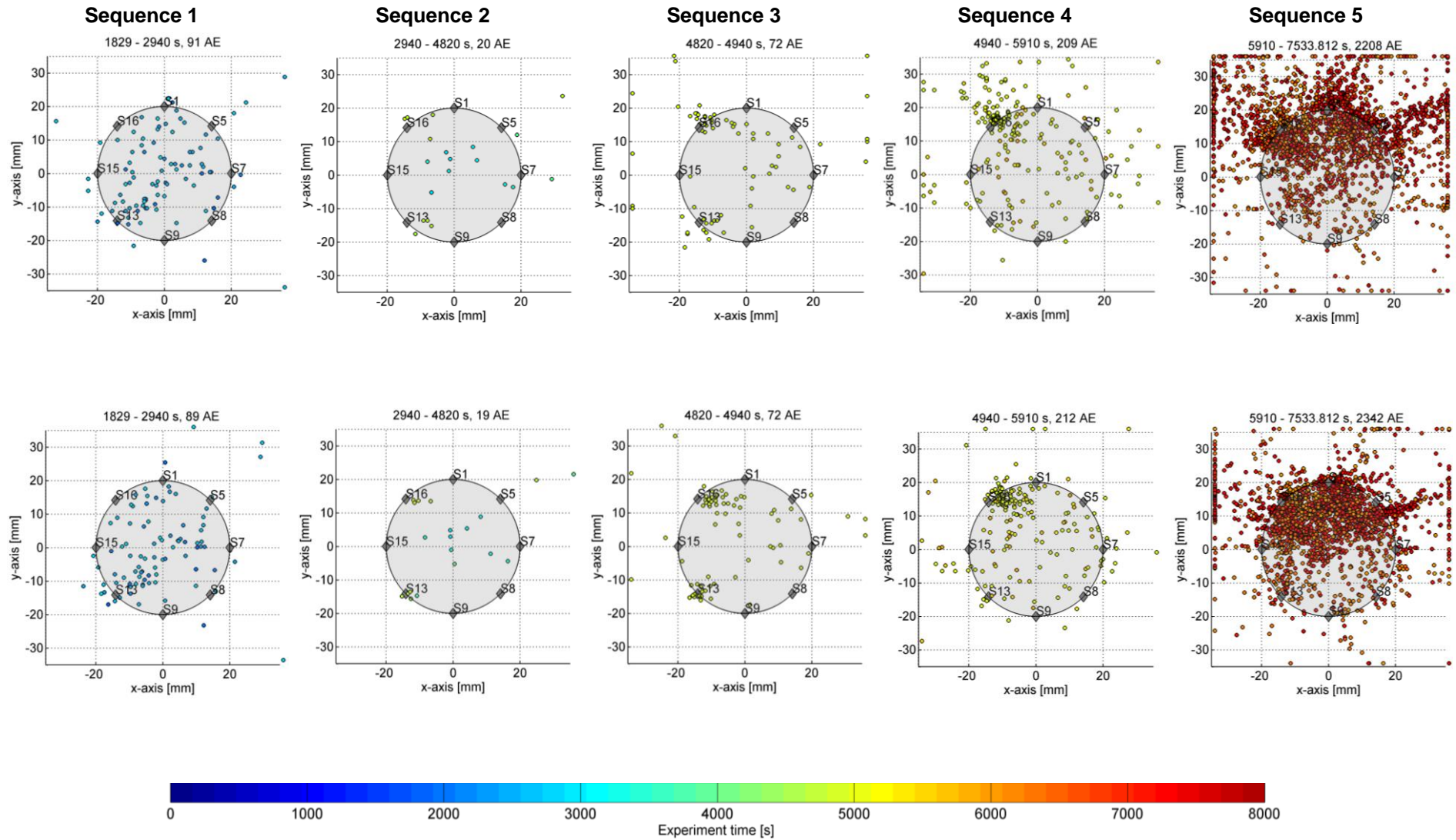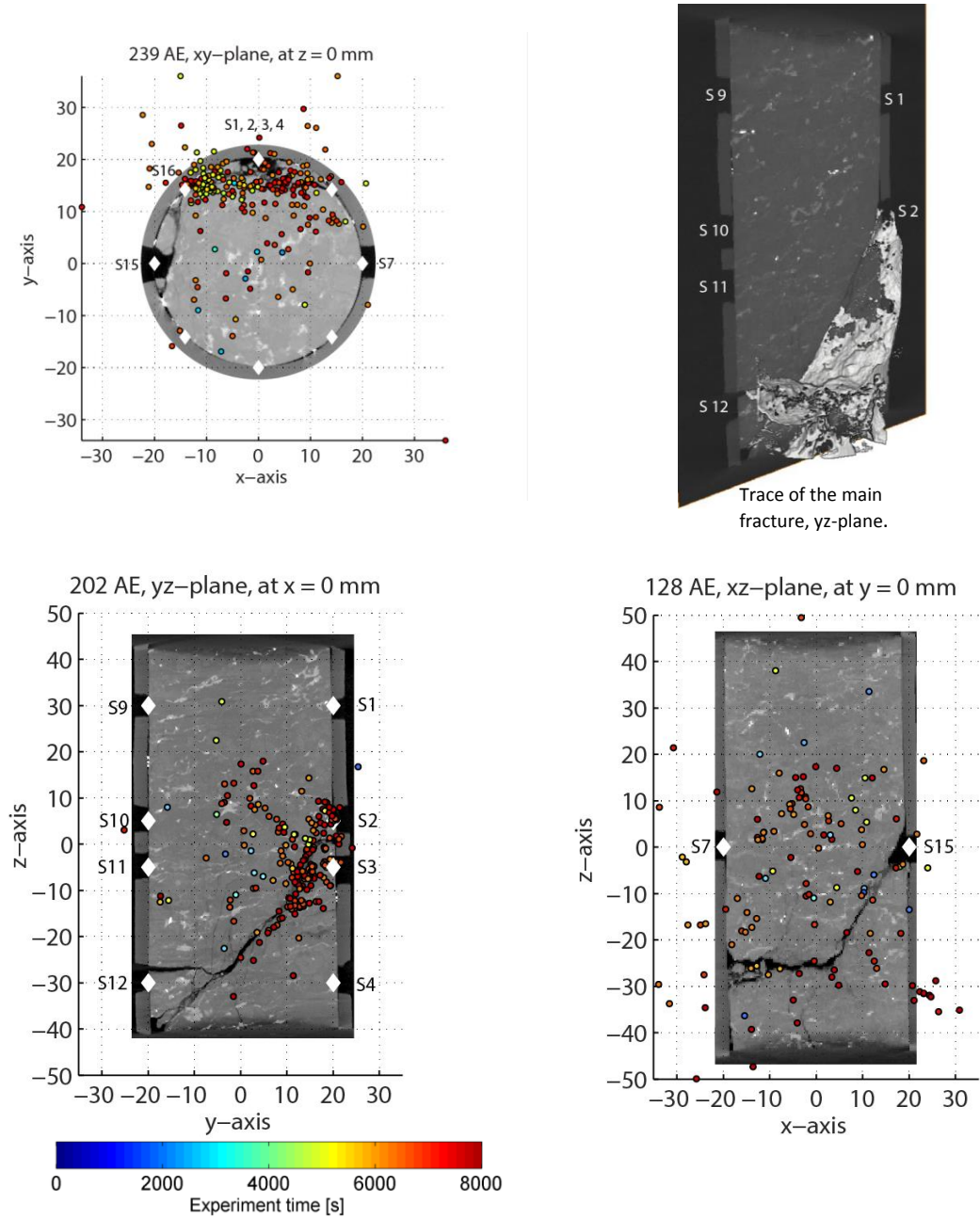Figure 4.14: Comparison AE (Ti-model implemented) to CT scan images. Sensor positions are marked with diamonds. CT scan images are aligned according to the sensors labeled.
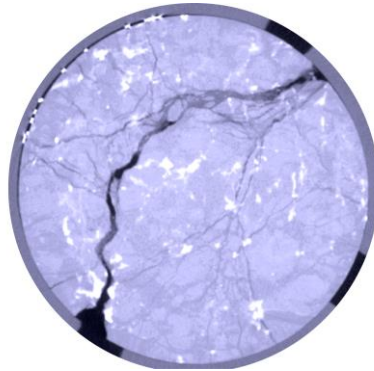

Figure 4.15: xy-plane at $z = -15\ mm$ of distinguished macroscopic fracture and fine coalesced microcracks.

4.3.4. Magnitude-frequency b-values

The b-value analysis are conducted for the frequency-magnitude distribution (FMD) of the 2000 events located inside the granite cylinder. The magnitude of completeness was determined using the Goodness-of-fit test (GFT). The b-values were obtained using the maximum-likelihood technique.
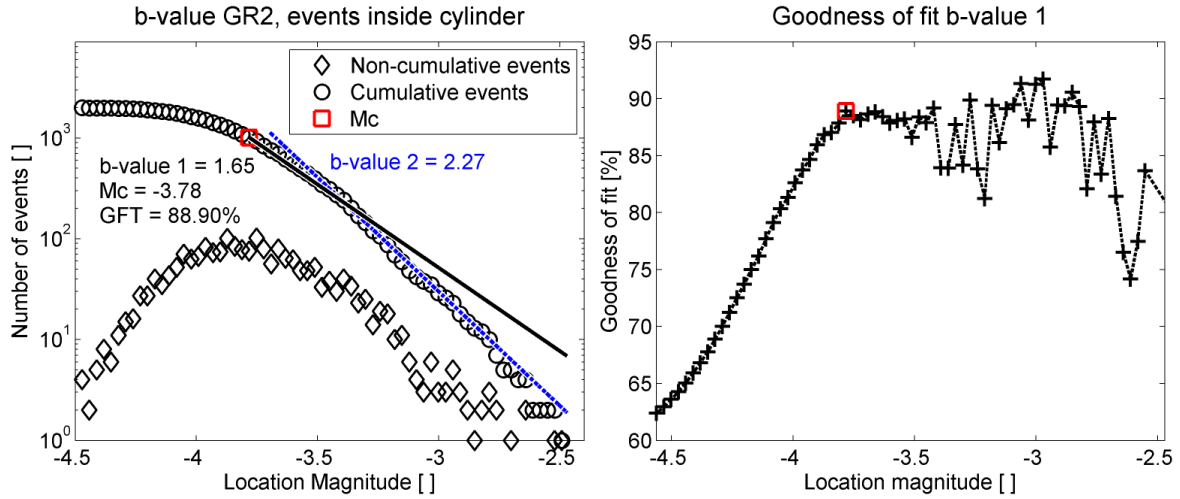

Figure 4.16: The b-values obtained over all foreshocks localized inside the granite cylinder.

Over all localized foreshocks a magnitude of completeness (M_c) of -3.78 was obtained at a goodness of fit quality of 88.9 % which reveals a b-value of 1.65. A second, lower b-value of 2.27 could be estimated in the second part of the FMD.

Taking a look at Figure 4.17 reveals the time dependent trend of b over the experiment. All events additionally to their magnitudes are shown. Number of high magnitude events increase towards failure. Calculating Mc time dependent using a moving window approach reveals a tendency to an increase in Mc towards the end of the experiment. Overall, the corresponding b starts low, increases with ongoing experiment and reveals the well-known drop towards failure of the sample (Lockner, 1993). Taking a closer look at b reveals two spikes. The b decrease at [1] is induced by the differential stress increase after $4\,800\,s$. The b-value increase at [2] is a result of an M_c increase, resp. a goodness of fit quality decrease below 86 %.

48
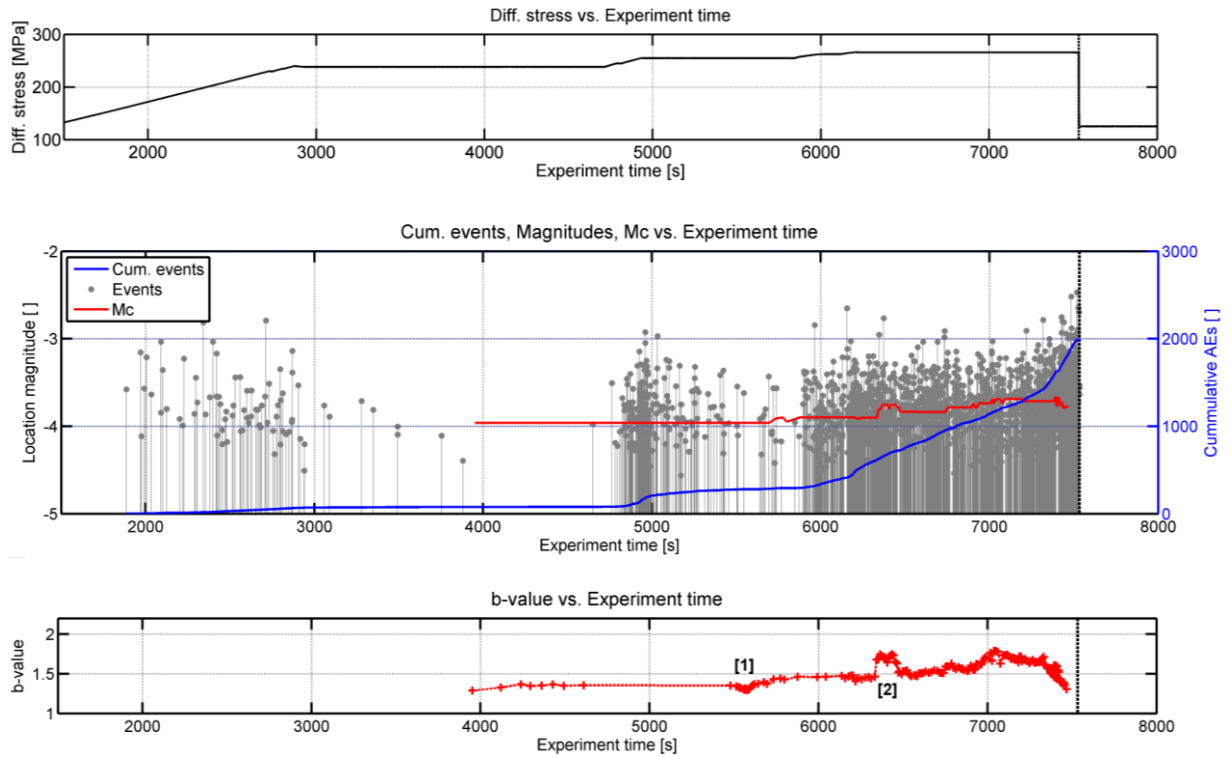
Figure 4.17: b-values over experiment GR2. Moving window settings (step size: 10, number of events per calculated Mc/b-value: 350, bin width: 0.05). Values of Mc and b are plotted in the center (time wise) of each particular moving window.

4.3.5. Accuracy of localization

To estimate an absolute accuracy in localization survey shots were picked manually and localized using collapsing grid search algorithm and implemented Ti-model. Sensors which recorded poor waveform quality or failed because macroscopic fractures formed in proximity during the ongoing experiment were not taken into account.

Figure 4.18: Absolute localization accuracy manual picked P-wave arrivals. Sensor 1 and 9 are placed in regions with poor sensor coverage. Sensor 2, 6, 8, 11 and 14 are placed within $\pm\,15\,mm$ of center of the sample. Error bars represent an error estimation of the localized shot according the Section 3.4.7.
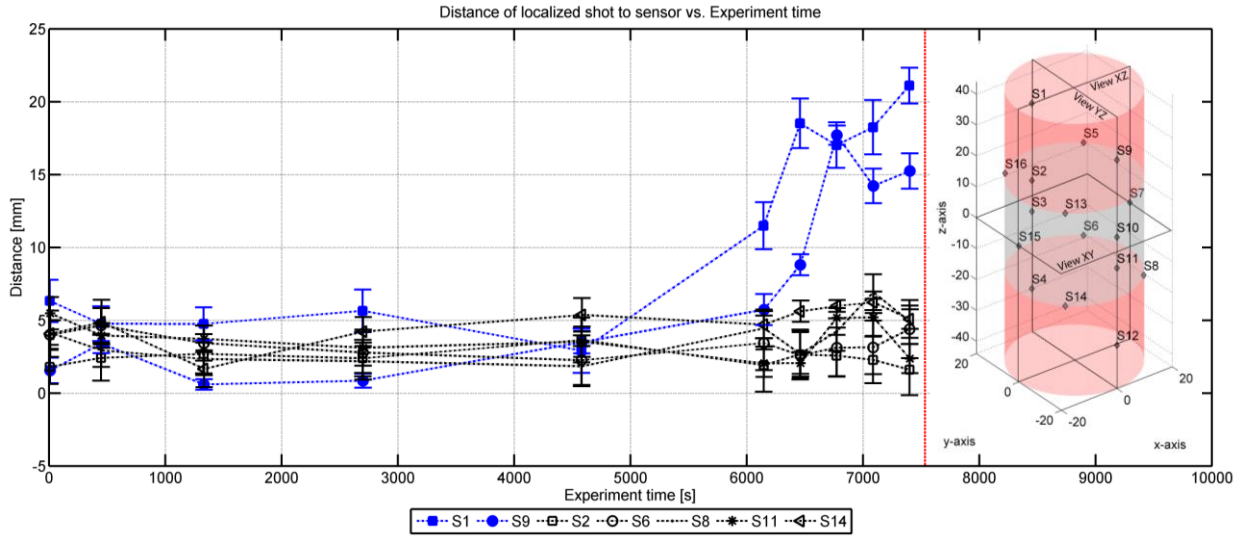
Within $\pm\,15\,mm$ of the sample center (grey volume, Figure 4.18) absolute localization accuracy is $\pm\,8\,mm$. Outside (red volumes, Figure 4.18), absolute localization accuracy decreases to $\pm\,22.5\,mm$ as microcrack density increases. Included here is the estimated localization error between measured and theoretical travel times (error bars).
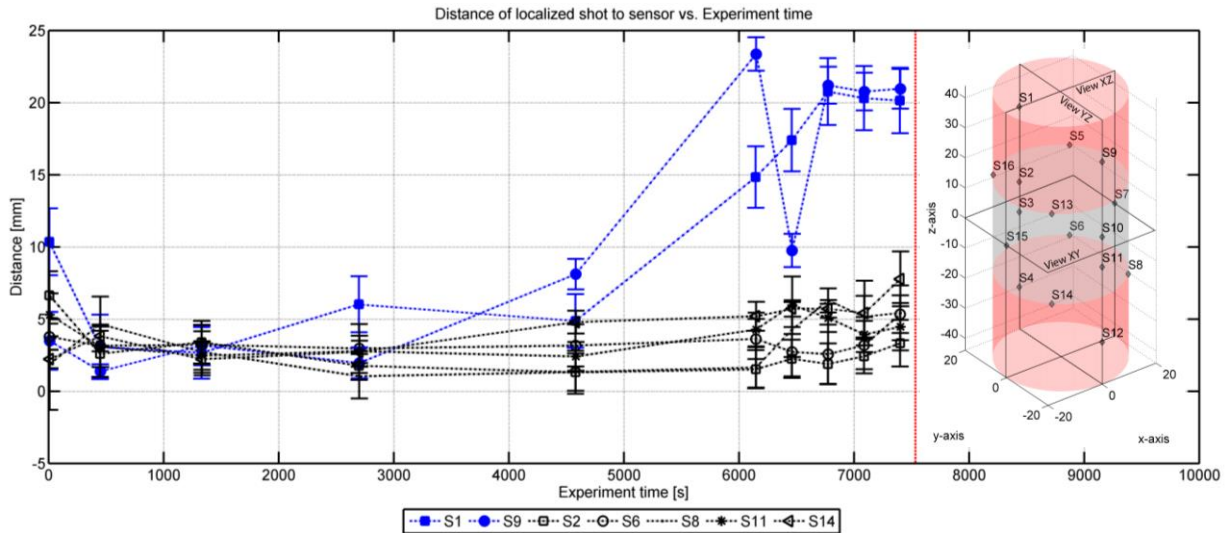
Figure 4.19: Absolute localization accuracy automatic picked P-wave arrivals. Sensor 1 and 9 are placed in regions with poor sensor coverage. Sensor 2, 6, 8, 11 and 14 are placed within $\pm\,15\,mm$ of center of the sample. Error bars represent an error estimation of the localized shot according the section 3.4.7.

In Figure 4.19 events were automatically picked and localized. The tendency holds, with increased microcrack density the accuracy of shots outside the center region increases to over $\pm\,20\,mm$. Location accuracy within the center region amounts in up to $\pm\,10\,mm$. What can be stated is that the Ti-model represents the occurrences equally well throughout the experiment.

4.4. Hydraulically induced AE, unconfined hydrofracture experiments

During experiment HF1 and HF2 granitic rock samples ($\varnothing$ 63.4 x 126 mm) were loaded to an axial stress of 3.1 MPa. Water was injected into an injection borehole 25 mm apart of a production borehole (see also Section 3.1.3). The purpose of the experiment was to increase permeability between the two boreholes. AE were recorded and opposed to injection pressure, injection rate and radial strain. Different amplification levels between the trigger sensor and the rest of the sensors made localization of events impossible. Only waveforms recorded at the trigger sensor revealed sufficient quality and were used for further analysis. Assuming all events distributed in proximity to the injection borehole a magnitude has been assigned to each event which allowed an estimation of b-values over pressure cycles.

4.4.1.   Experiment HF1

For HF1 injection lasted one pressure cycle. The end of a cycle is determined by reaching the breakdown pressure. Breakdown pressure was reached at 55 bar were injection rate amounts in 135 ml/min and global radial strain was 0.014 %. A total of 541 acoustic events were counted, whereas AE rate starts to increase prior to failure (Figure 4.20).
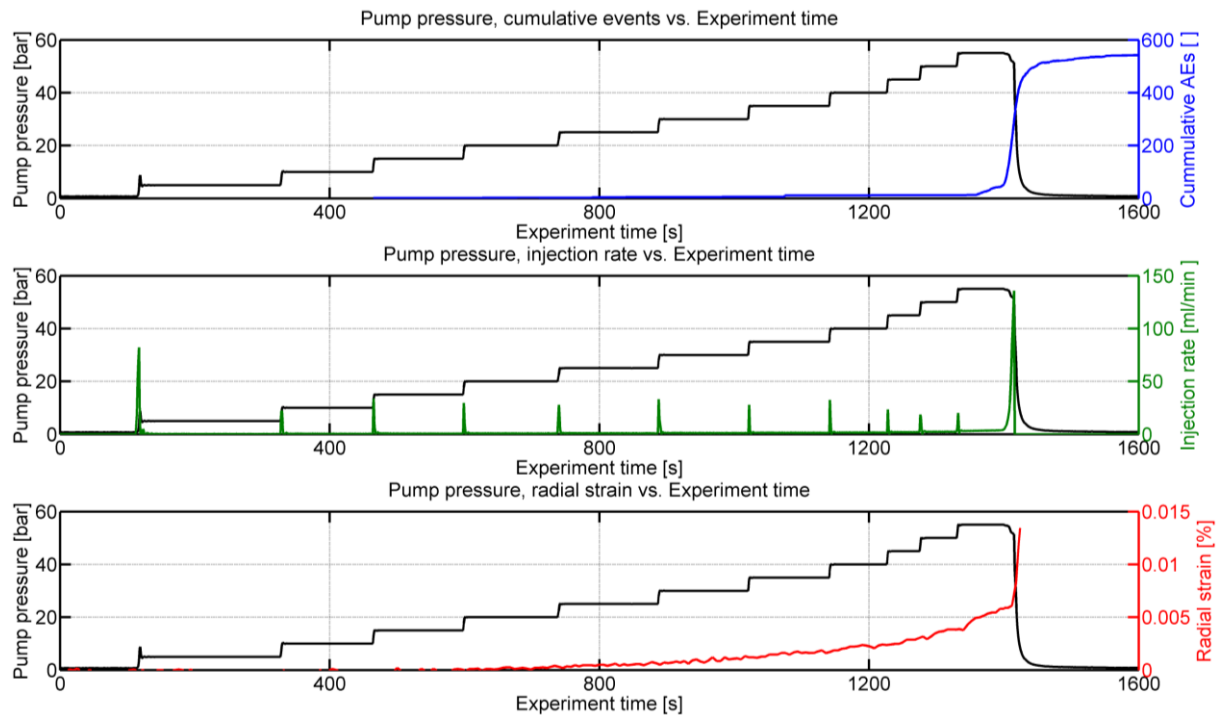

Figure 4.20: Overview HF1 over one cycle

HF1 was equipped with four strain gauge patches measuring local axial and radial strain (Figure 4.21).

51
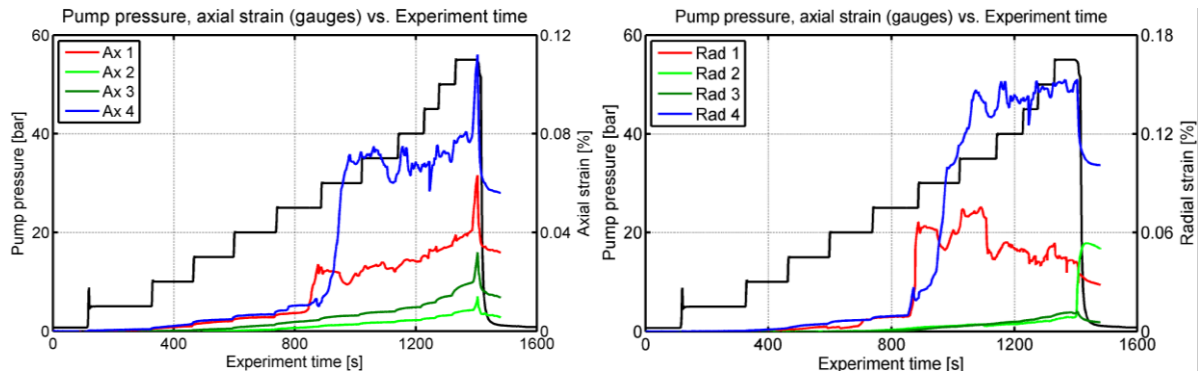
Figure 4.21: Overview strain gauges. Each patch (1-4) consists of an axial and a radial strain gauge.

Local deformation follows pressure steps, after $850\,s$ strain gauge patch 1 and 4 diverge. Non-hydrolysis resistant instant adhesive is seen as possible reason for loosening strain gauge patches.

4.4.2. Experiment HF2

HF2 injection lasted three pressure cycles (Figure 4.22). Breakdown pressure was reached at $90,\,84.7,\,83.8\,bar$, while injection rate amounted in $36,44,88\,ml/min$. Radial strain was 0.008 % higher after the first cycle compared to the original circumference before fluid injection, increased to 0.010 % after the second cycle and became 0.011% after the third cycle. Acoustic emission increased by 1300 events after the first, by 1260 events after the second and by 1000 events after the third cycle. Prior to breakdown pressure of all cycles, AE rate starts to increase. With a short sequence of aftershocks AE rate decreases to zero after break down pressure was reached.
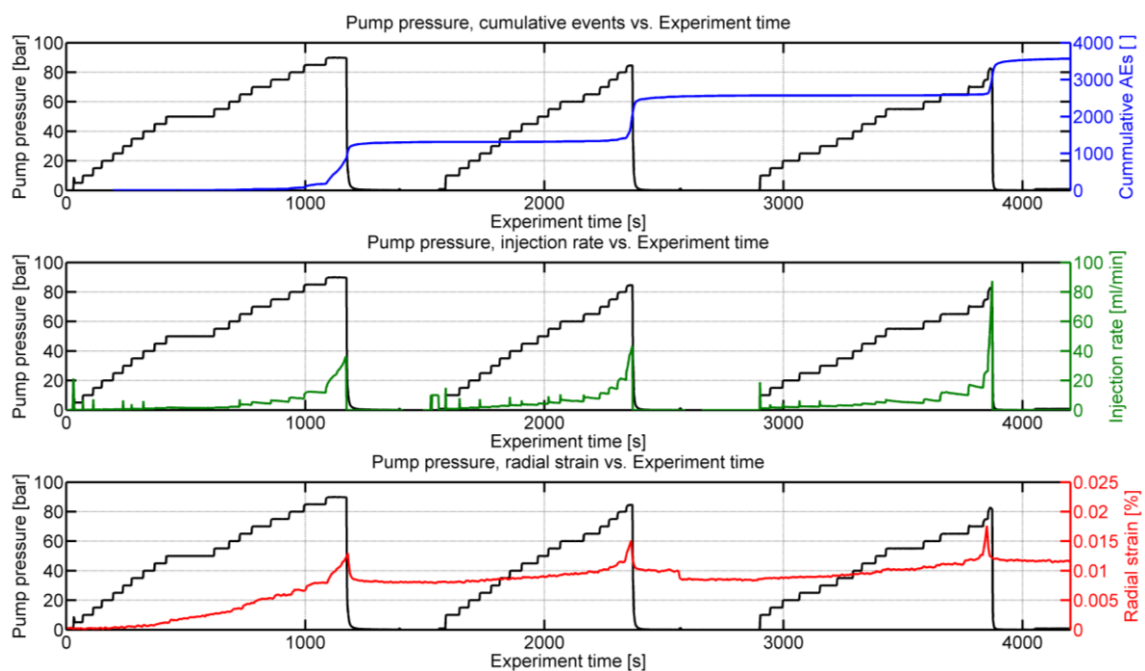
Figure 4.22: Overview HF2 over 3 cycles

Computing pressure vs. injection rate reveals an increasing injectivity after each cycle (Figure 4.23).
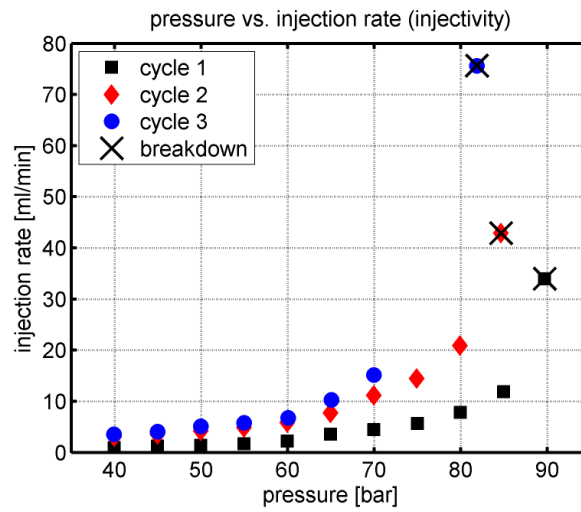
Figure 4.23: HF2 Injectivity over three pressurization cycles starting at 40 *bar*, increases in 5 bar increments and ends at the break down pressure of each cycle.

4.4.3.   Magnitude-frequency b-values

As mentioned earlier, localizing recorded events was not possible because of different amplification levels at sensors. Determining peak amplitudes of waveforms recorded by the trigger sensor additionally to the assumption that each event has the same distance (i.e. the radius of the granite sample) to the receiving trigger sensor (sensor 1, Section 3.1.3, Figure 3.6) a magnitude was calculated which in turn allowed an estimation of b-values over pressure cycles.
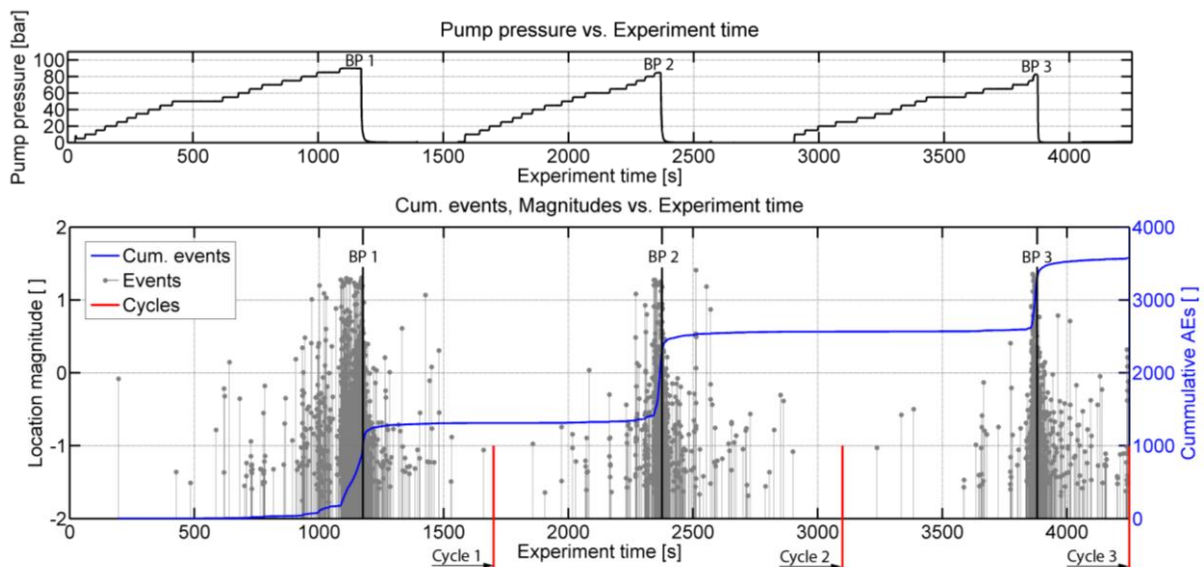
Figure 4.24: Cycles of AE recorded over the three pressure cycles. Low AE activity after break down pressure was reached determines a cycle.
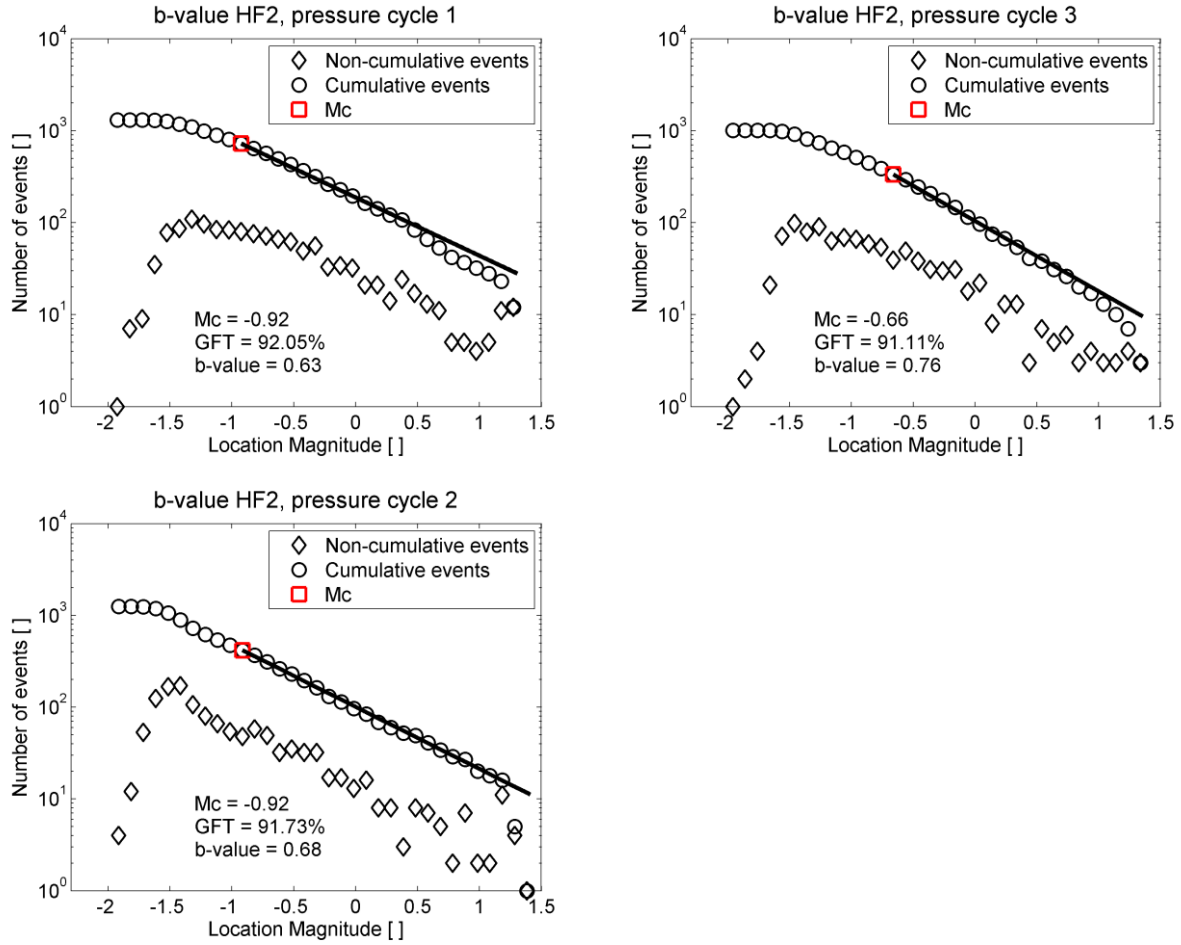
Figure 4.25: b-values over three pressure cycles indicated in Figure 4.24. M_c was calculated using the goodness of fit test, b's were estimated by the maximum-likelihood technique.

b-values over the three pressure cycles (Figure 3.5) reveal to be in the same order of magnitude. A slight increase in b can be estimated with every repeated pressure cycle. Mc's are determined at goodness of fit qualities of at least 90%.
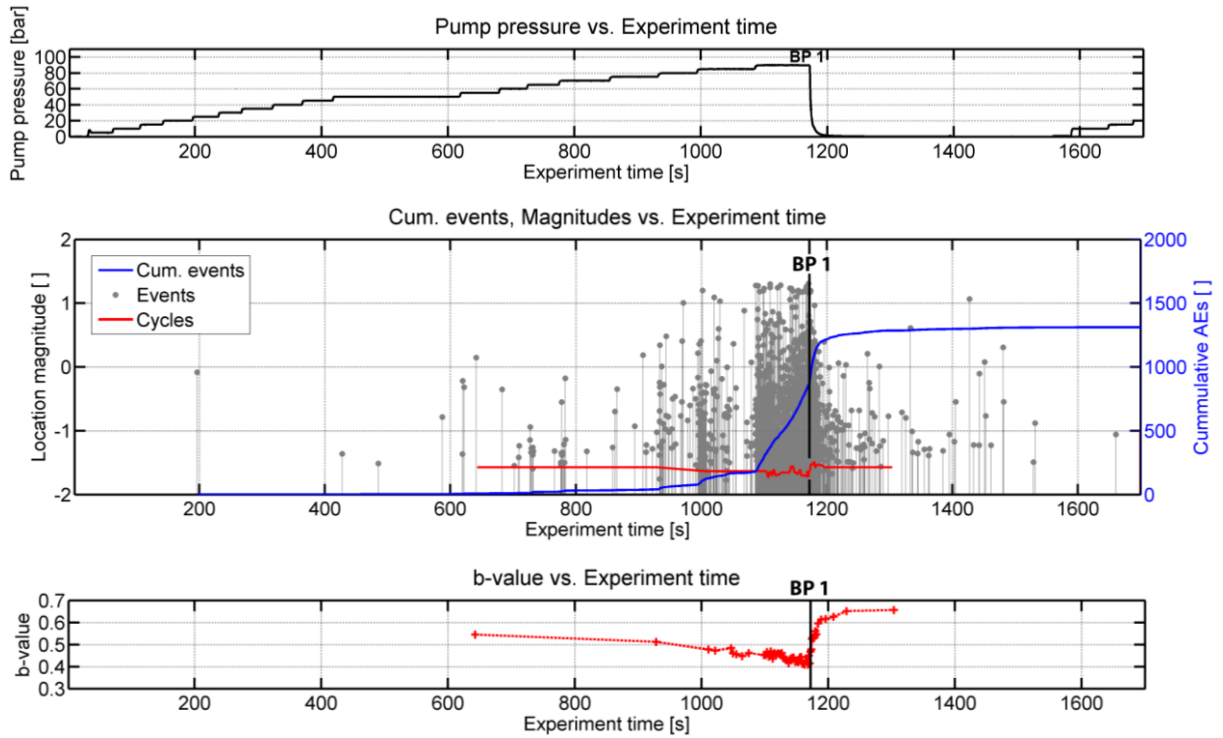
Figure 4.26: b-values over pressure cycle 1. Moving window settings (step size: 20, number of events per calculated Mc/b-value: 200, bin width: 0.1). Values of Mc and b are plotted in the center (time wise) of each particular moving window.

Figure 4.26 shows b-values time dependent using a moving window approach over pressure cycle 1. b starts at 0.55 and drops towards break down pressure to 0.41. After the pressure release b-values increase with a steep slope to 0.66. Mc shows a slight decrease towards breakdown pressure, at breakdown pressure Mc increases. The goodness of fit quality throwout the cycle is comparably low with at least 83 %. Over pressure cycle 2 and 3 b-values show similar characteristics.

5. Discussion and conclusion

Experiments conducted within the framework of this thesis began as research efforts in the field of laboratory-scale acoustic emissions (AE) within the SCCER at ETH Zurich. Basic knowledge in the field of AE during brittle failure of rock on a laboratory scale was limited, as were the necessary technical resources. Therefore, fundamental research was undertaken to set a baseline for the development of future cutting-edge research in this field.

Experiments conducted at ESN in Paris using a well-equipped apparatus allowed the experimenter to take essential steps towards a complete catalogue of AE recorded during two differential-stress induced seismicity experiments. The use of the commercially available analysis software InSite (Consultants, 2014a) permitted the management of the vast amount of recorded data in a relative straightforward manner. Two interconnected acquisition system at ETH Zurich formed the core of the experimental apparatus with which two subsequent hydraulically induced AE experiments were conducted. This work forms the foundation for further scientific work in the field of localizing AE during failure of rock on a laboratory scale here at ETH Zurich.

In the first part of this work cylindrical, granitic rock samples ($\emptyset\ 40\ x\ 88\ mm$) were axially compressed under triaxial conditions until failure occurred. Axial compressive stress, confining stress, axial and radial strain, as well as AE signals from 16 spatially distributed transducers, were recorded. Travel times were measured (i.e. surveys) between transducer pairs during the entire experiment in $300\ s$ intervals, using transducers as emitting sources. Calculated axial P-wave velocities towards the end of the experiment were up to 27% higher than P-wave velocities perpendicular to the axial direction (Section 4.3.2). For localizing AE, a time-dependent homogeneous-isotropic velocity model (Hi-model) was developed, using an average of P-wave velocities measured perpendicular to the cylinder axis. P-wave onsets of recorded AE were picked automatically by implementing the RMS amplitude method. To improve picking accuracy, only strong events that demonstrate a clear distinguishable P-wave onset were picked. Using a collapsing-grid-search algorithm with implemented Hi-model for localization, out of 5500 recorded foreshocks (i.e. AE before failure) only 1340 were localized inside the granite cylinder.

Advances were made toward estimating the absolute accuracy of localized AE by localizing shots emitted by transducers at known locations during surveys. Shots were picked manually to exclude automatic picking errors, and showed increased deviation from the transducer location especially in axial direction towards the end of the experiment. When automatically picked shots were localized, it became clear that deviation in location between shot and transducer was similar, which revealed the velocity model as the main reason for an inaccurate localization. A time-dependent transversely isotropic velocity model (Ti-model) was developed to take into account measured diverging velocities in an axial direction and perpendicular-to-the-axial direction. Velocities thereby vary by a function of time and ray path orientation through the volume with respect to the cylindrical axis (Consultants, 2014a). When survey survey shots with implemented Ti-model were localized the absolute accuracy throughout the experiment improved considerably compared to localizations using the Hi-model. An absolute localization accuracy of $\pm 10\ mm$ for strong events at the lateral surface of the granite sample which disposes of a high sensor coverage can be confirmed. Locally increased accuracy can be assumed inside the center region of the cylinder due to higher sensor coverage. Outside the sample region at low sensor coverage, localization accuracy for strong events at the lateral surface decreases to more than $\pm 20\ mm$ (Section 4.3.5, Figure 4.19).

To compare the achieved accuracy with state-of-the-art accuracies in similar experiments, it is useful to examine the work of Kwiatek et al. (2014). They performed stick-slip experiments on Westerly Granite samples ($\emptyset\ 40\ x\ 107\ mm$ resp. $\emptyset\ 50\ x\ 102\ mm$). Using 16 transducers and a time-dependent anisotropic velocity model updated every $30\ s$, they report an accuracy of $\pm 2\ mm$. Rock samples used in his study were prepared with notches, or smooth saw cuts, which limited the damage zone and allowed to establish an increased sensor coverage at the location of interest.

In order to improve localization accuracy, three main issues should be addressed:

(1) Automatic picking of P-wave onsets are erroneous. As stated earlier (Section 0), the location accuracy of automatically picked strong survey shots is in the same order of magnitude as manually picked shots, which suggest a negligible impact on localization accuracy.

(2) The velocity model does not represent the velocity distribution during triaxial compression adequately enough. Velocity measurements during the experiment suggest an increasing anisotropy as the experiment continuous. A high crack density visible on CT-scan images throughout the cross section of the sample (Section 4.3.3, Figure 4.15) further suggests heterogeneity.

(3) The deployed transducers also contribute to an accurate localization. For the triaxial compression experiment, self-made piezo-ceramic transducers encapsulated in a $7\ mm$ curved brass housing were used. The attached 7 mm face surface of the transducers to the rock sample can be questioned as point receivers/sources. Kwiatek et al. (2014) uses transducers of similar size, which suggests a small impact on localization accuracy.

These three points suggest that the implemented Ti-model does not adequately represent velocity distributions during a triaxial compression experiment. It can be concluded that, in order to achieve more accuracy in localizing AE recorded during triaxial compression experiments where an increased microcrack density or even fluid penetration is expected, time-dependent, heterogeneous and anisotropic velocity models are desirable. Implementing such a velocity model is beyond the scope of this work, and the Ti-model was used for further analyses.

The implemented Ti-model leads to 2000 foreshocks localized inside the granite cylinder. The localized foreshocks made microcrack initiation, fault nucleation and fault propagation visible (Section 4.3.3, Figure 4.12). In addition, the location of failure determined by AE is in great agreement with CT-scan images (Section 4.3.3, Figure 4.13).

Knowing the location of an AE, a magnitude can be assigned to it on an experimentally specific scale. Magnitudes represent an estimation of the strength of an event and are calculated according to maximum amplitudes recorded at each transducer. Assigning the Gutenberg-Richter power law (GR) to cumulative events of binned magnitudes lead to the b-value that represents the relative proportion of small vs. large events. The frequency-magnitude distribution (FMD) of the $2\ 000$ events localized inside the granite cylinder seems to follow the GR according to two different trends. Below a magnitude of -3.3 a low b-value of 1.65 can be assigned; above a higher b-value of 2.27, the GR fits best (Section 4.3.4, Figure 4.16). This suggests an incomplete or mixed catalogue. The selection process which led to the $2\ 000$ events inside the cylinder is seen as a possible reason for the two different b-values. In total, $5\ 450$ foreshocks are recorded (red line, Figure 5.1). The following selection criteria are then applied and lead to the $2\ 000$ selected events: (1) Conservative automatic picking settings lead to a selection of events providing steep slope onsets of P-waves. (2) Erroneous P-wave picks, combined with the influence of an inaccurate velocity model, result in localization residuals exceeding the set threshold. A combination of criteria 1 and 2 leads to all the events located during the experiment (green line, Figure 5.1). (3) Only events located inside the cylinder volume are considered (blue line, Figure 5.1).

What remains striking is that the three colored lines (Figure 5.1) diverge as the experiment continuous. This means a decreasing number of events are localized. In addition, an increasing number of events are localized outside the granite cylinder.
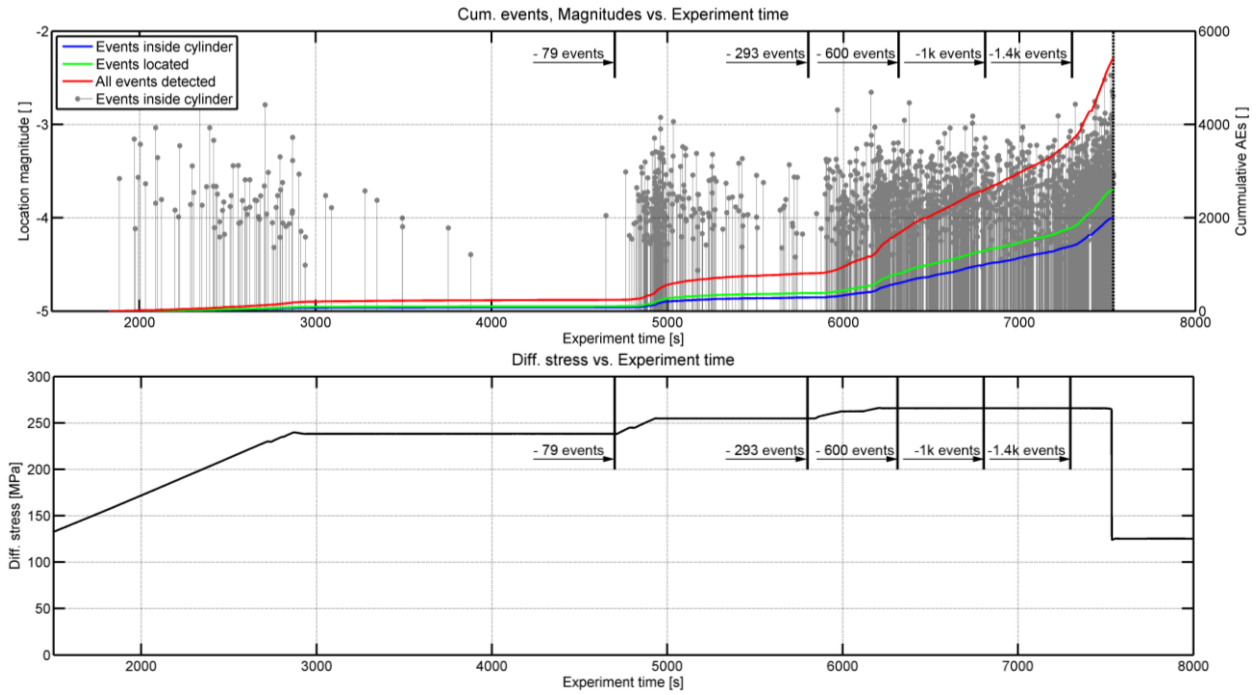

Figure 5.1: Event distribution including cumulative number of all detected foreshocks (red line), located foreshocks (green line) and foreshocks located inside the granite cylinder (blue line).

It is difficult to determine what selection criteria contribute to what extent to the possible incomplete catalogue of 2 000 events. Moreover, it is not possible to estimate to what extent the two b-values represent physical occurrences during triaxial compression. However, it can be concluded that the two b-values already appear at an early stage in the experiment. Figure 5.2 shows calculated b-values for cumulative event sections. Two b-values can already be estimated in the FMD of Event 1-to-293. When FMDs are expanded with further events (more than 600), goodness-of-fit quality decreases to values lower than 89 %. At the same time, the magnitude of completeness increases with ongoing experiment.

An increasing Mc also appears in the time-dependent FMD analysis using a moving window approach (Section 4.3.4, Figure 4.17). Time-dependent b-values range between 1.28 and 1.79, which reveals results similar to the bs obtained over cumulative event sections. Finally, a higher number of experiments, a more advanced P-wave picking method, and a more accurate velocity model would be needed to be able to distinguish between analysis-specific effects and physical occurrences.
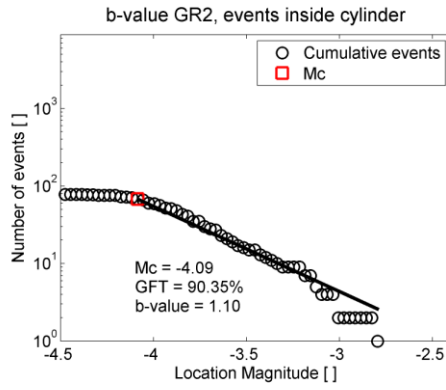
Event 1 – 79
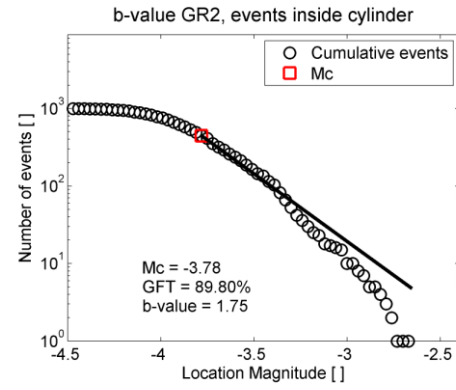
Event 1 – 1000
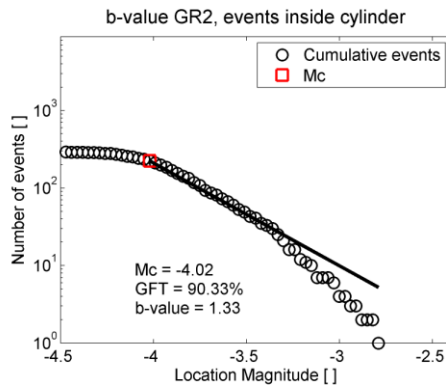
Event 1 – 293
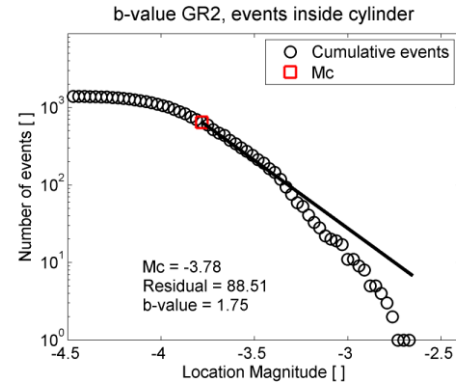
Event 1 – 1400
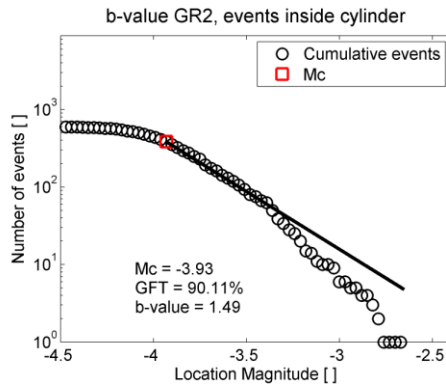
Event 1 – 600
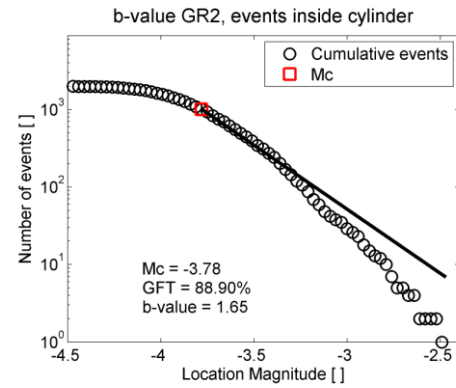
Event 1 – 2000

Figure 5.2: b-values calculated for different event sequences starting with event number 1. Time intervals of event sequences are shown in Figure 5.1.

In the second part of this thesis, cylindrical granitic rock samples ($\emptyset\ 63.4\ x\ 126\ mm$) were exposed to hydraulic injection pressure under uniaxial loading. Injection pressure was applied using an injection nozzle to boreholes drilled perpendicular to the cylinder axis, $25\ mm$ apart from each other. This configuration represents a new experimental setting in this type of hydraulically induced seismicity experiments. Pressure steps were performed in $5\ bar$ incre-

ments until break-down pressure was reached. Break-down pressure was reached in three repeated cycles.

Evidence for irreversible deformation was given by an increased radial strain level (measured by extensometer, Section 3.2.2) after each cycle. Further evidence for deformation was revealed through an increased injectivity (i.e. a higher injection rate at lower injection pressure) with each cycle (Section 4.4.2, Figure 4.23). Visual observation during the experiment just before breakdown pressure was reached showed fluid discharge through openings randomly distributed at the surface area of the cylinder $\pm 20\ mm$ around the injection borehole. No fluid flow was recognized at the production borehole (located $25\ mm$ apart from the injection borehole), which suggests no increased permeability between the boreholes. It is assumed that the applied axial stress field (σ_1) was insufficiently high to allow directed microcracking between the two boreholes.

CT-scan images at a resolution as low as $33\ \mu m$ taken after fluid injection revealed no recognisable fractures. This suggests that induced hydraulic fractures in an unpressurised state are smaller than $33\ um$. It is assumed that deformation is partially quasi-elastic and that fractures partially close after fluid pressure is released.

It proved difficult to interconnect AE acquisition systems. Sufficient AE waveform quality was only recorded at the trigger sensor. However, acoustic emission analysis revealed a decrease of total AE with each performed and repeated cycle. Estimated b-values over single cycles prove to be in the same range, with a slight increase occuring with repeated cycles. This suggests a decrease of deformation potential with each cycle and decreasing backpressure. The time dependent b shows a decrease with increasing breakdown pressure and porves lowest at breakdown pressure. This b-value characteristic is repeated over the different pressure cycles. bs must be interpreted with care, as magnitudes of AE are based on recorded maximum amplitudes at only one sensor and an equal location of all events. For further investigation of hydraulically induced seismicity, a more elaborated AE acquisition system allowing the localization of AE is needed. Increasing the axial stress field (σ_1) could contribute to directed microcracking and permeability creation between the two boreholes.

The following main conclusions can be drawn from this work:

- Localization of AE in brittle failure of rock:
    - The application under confined conditions of axial compressive stress until the point of failure to a cylindrical granite sample causes increasing microcrack

density, which in turn leads to time dependent, heterogeneous and anisotropic seismic velocity distributions.

- An accurate modeling of occurring heterogeneities and anisotropies in seismic velocities plays an essential role in the accurate localization of AE emitted during brittle failure of rock.

- High sensor coverage at location of interest increases the accuracy of localization.

- Differential-stress-induced seismicity in triaxial compressed granite samples:
  - Temporal b-values start low, increase with ongoing experiment and reveal the well-known drop towards failure of the sample.

- Injection-induced seismicity in uniaxial loaded granite samples:
  - Applying injection pressure to axially loaded granite samples until break-down pressure is reached leads to irreversible deformation.
  - Temporal b-values over a pressure cycle decrease with increasing injection pressure and are lowest at breakdown pressure.

This work makes a small but significant contribution to the broad field of induced seismicity on a laboratory scale. If the reader should be left with one crucial thought for the future, it is the importance of knowing the localization error for each AE which is necessary for all subsequent associated analyses. Also, the repeatability of results needs to be ensured with multiple experiments under equal conditions. Possible future research topics and experiments follow in Section 6.

6. Outlook

An accurate localization of AE during brittle failure of rock forms the top priority for any further experiments conducted in the field of EGS on a laboratory scale. Obtaining an increased accuracy in localization permits advanced analysis, such as the tracking of propagating fractures or spatial b-value mapping, which could contribute towards a better understanding of physical processes that lead to induced seismicity.

Developing an accurate model that describes heterogeneities and anisotropies in seismic velocities during fluid penetration and increased microcrack density is the main challenge that should be addressed in the future. One possible approach to advance this challenge is to analyse P-wave travel times obtained during surveys with classical tomography techniques. A three-dimensional velocity model disposing of discrete volume blocks of different seismic velocities would be the outcome. Schubert (2006) introduced another promising technique to develop heterogeneous and anisotropic velocity models and increase localization accuracy of AE. He suggests a combination of a localization algorithm and a tomography algorithm and is able to use recorded AE as tomographic point sources. Assuming 1000 AE received by 16 sensors, it is possible to observe 1600 travel times within 1600 spatially distributed ray paths. In addition, travel time measurements, or, in other words, surveys are no longer needed.

Improving the procedure of automatic P-wave picking represents another step toward an accurate localization and a complete catalogue of AE during an experiment. A suggestion would be to classify AE according to the signal-to-noise ratio of waveforms. This would allow automatic picking algorithms individually adjusted.

Deploying calibrated sensors would permit the estimation of physical magnitudes of AE, which would facilitate experiment-comprehensive examination as well as improve upscaling attempts.
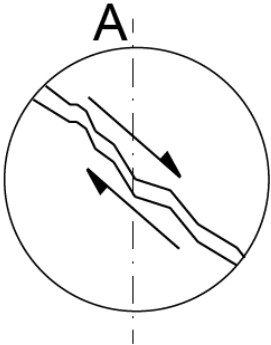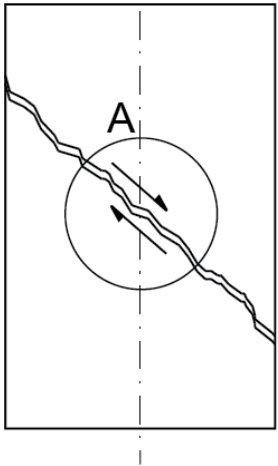
Finally, adequate software and hardware is needed which makes it possible to combine all the aforementioned issues.
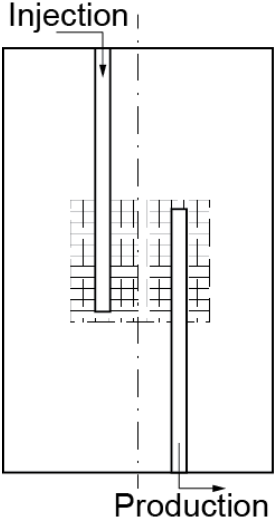
6.1. Possible future experiments

A variety of hydraulic injection experiments on a laboratory scale at EGS-relevant conditions (temperature $> 180\,°C$, lithostatic pressure $> 100\,MPa$) are suggested in order to understand processes which lead to hydraulically induced seismicity during permeability creation. Frac-

ture mechanical properties and hydraulic properties connected to AE characteristics are of interest. Suggested research topics and experiments assume the purchase of an internally heated triaxial cell, providing the possibility of fluid injection, in addition to the introduction of acoustic emission equipment.

The following research topics and experiments under EGS-relevant conditions can be addressed:

Microscopic fracture mechanical properties: 	• Observation of fracture mechanical parameters. - Fracture toughness with different temperature and deviatoric stress, in combination with thermomechanical effects (tensile tests under triaxial condition).

Macroscopic fracture mechanical properties:
 	
	• Inducing hydraulic fractures at different deviatoric stress levels and different temperatures.
	• Hydraulic reactivation of shear faults.
	  - Influence of fracture orientation. How do misoriented fractures behave in relation to hydraulic reactivation?
	  - Influence of fracture surface (Sawed, ground, triaxially generated, with and without gouge).
	  - Observation of rate-and-state frictional properties after onset of slip.
	  - Observation of transition from aseismic to seismic slip
	  - Changes in temporal and spatial b-values and stress drop, depending on fracture orientation and fracture surface condition.
	  - Influence of thermo-mechanical effects on fault reactivation.

| Small-scale analogue EGS:

Injection

Production | • Laboratory scale analogue EGS, (1) laboratory-scale stimulation, (2) circulation of fluid, (3) heat extraction

 - Influences of thermo-mechanical effects associated with cold-water injection on induced seismicity and permeability creation.

 - Influences of the injection program (varying injection rates) on permeability creation and magnitudes of occurring events (b-values).

 - Temporal variation in permeability of generated fractures (chemical dissolution, mechanical deformation of self-propping asperities).

 - Quantification of heat exchange between fluid and rock.

• Validation/calibration of numerical models

• Real time AE location during an experiment |
| Upscaling:

 | • Connecting laboratory-scale observations with observation of large scale injection experiments (e.g. hydraulic-shearing experiment at GTS).

• Design strategies which can limit induced seismic hazard during permeability creation deep underground. |

The author hopes further research along these lines will continue.

Bibliography

Bachmann, C. E., Wiemer, S., Woessner, J., & Hainzl, S. (2011). Statistical analysis of the induced Basel 2006 earthquake sequence: introducing a probability-based monitoring approach for Enhanced Geothermal Systems. *Geophysical Journal International, 186*(2), 793-807. doi: 10.1111/j.1365-246X.2011.05068.x

Barbara, S. (2005). *Schallemissionsanalyse zur Überwachung der Schädigung von Stahlbeton.* ETH, Zürich.

Brace, W. F., & Byerlee, J. D. (1966). Stick-Slip as a Mechanism for Earthquackes.

Brantut, N., Heap, M. J., Meredith, P. G., & Baud, P. (2013). Time-dependent cracking and brittle creep in crustal rocks: A review. *Journal of Structural Geology, 52*, 17-43. doi: 10.1016/j.jsg.2013.03.007

Burg, J.-P. (2015). Sprödbruchbildung.

Charalampidou, E.-M., Stanchits, S., Kwiatek, G., & Dresen, G. (2014). Brittle failure and fracture reactivation in sandstone by fluid injection. *European Journal of Environmental and Civil Engineering, 19*(5), 564-579. doi: 10.1080/19648189.2014.896752

Consultants, A. S. (2014a). InSite User Manual v3.3.0.

Consultants, A. S. (2014b). Richter 16 Data-Acquisition Unit User Manual.

Consultants, A. S. (2015). InSite User Manual v3.5.0 TECHNICAL APPENDIX.

Goebel, T., Becker, T. W., Schorlemmer, D., Stanchits, S., Sammis, C., Rybacki, E., & Dresen, G. (2012). Identifying fault heterogeneity through mapping spatial anomalies in acoustic emission statistics. *Journal of Geophysical Research: Solid Earth, 117*(B3), n/a-n/a. doi: 10.1029/2011jb008763

Goebel, T., Sammis, C. G., Becker, T. W., Dresen, G., & Schorlemmer, D. (2013). A Comparison of Seismicity Characteristics and Fault Structure Between Stick–Slip Experiments and Nature. *Pure and Applied Geophysics.* doi: 10.1007/s00024-013-0713-7

Hirschberg S., e. a. (2015). Energy from the Earth.

Holcomb, D. J. (1986). Setecting Damage Surfaces in Brittle Materials Using Acoustic Emissions.

Jaeger, J. C., Cook, N. G. W., & Zimmerman, R. W. (2007). Jaeger Fundamentals of Rock mechanics.

Kraft, T., & Deichmann, N. (2014). High-precision relocation and focal mechanism of the injection-induced seismicity at the Basel EGS. *Geothermics, 52*, 59-73. doi: 10.1016/j.geothermics.2014.05.014

Kwiatek, G., Goebel, T. H. W., & Dresen, G. (2014). Seismic moment tensor andbvalue variations over successive seismic cycles in laboratory stick-slip experiments. *Geophysical Research Letters, 41*(16), 5838-5846. doi: 10.1002/2014gl060159

Lei, X.-L., Li, X.-Y., & Li, Q. (2014). Insights on Injection-induced Seismicity Gained from Laboratory AE Study Fracture Behaviorbof Sedimentary Rocks.

Lockner, D. (1991). Quasi static fault growth and shear fracture energy in granite.

Lockner, D. (1993). The Role of Acoustic Emission in the Study of Rock Fracture.

Lockner, D. A., & Beeler, N. M. (2002). Rock Failure and Earthquakes *International Handbook of Earthquake and Engineering Seismology* (pp. 505–537). New York: Elservier.

McClure, M. (2014). Characterizing Hydraulic Fracturing With a Tendency-for-Shear-Stimulation Test.

McLaskey, G. C., & Glaser, S. D. (2012). Acoustic Emission Sensor Calibration for Absolute Source Measurements. *Journal of Nondestructive Evaluation, 31*(2), 157-168. doi: 10.1007/s10921-012-0131-2

Olympus. (2015). Schallgeschwindigkeiten im Material. Retrieved 01.07, 2015

Passelègue, F. X. (2014). *Étude Expérimentale de la Rupture Sismique.* (Ph.D.), École Normale Supérieure Paris

Preisig, G., Eberhardt, E., Gischig, V., Roche, V., van der Baan, M., Valley, B., . . . Lowther, R. (2015). Development of connected permeability in massive crystalline rocks through hydraulic fracture propagation and shearing accompanying fluid injection. *Geofluids, 15*(1-2), 321-337. doi: 10.1111/gfl.12097

Research, S. C. C. f. E. (2015). *2015*(12.02.2015). Retrieved from: http://www.sccer-soe.ch/opencms/opencms/research/geo/

Sause, M. G. R. (2011). Investigation of pencil-lead braks as acustic emission sources.

Schubert, F. (2006). Tomography techniques for acoustic emission monotroing.

Services, K. (2011). 'SteveCo' KRNBB-PC Point Contact Sensor.

Solberg, P., Lockner, D., & Byerlee, J. (1977). Shear and Tension Hydraulic Fractures in Low Permeability Rocks.

Tester, W. (2006). The future of geothermal energy, MIT.

Warner, M., & Laura, S. (2003). A review and insights on the estimation of the b-value and its uncertainty.

Wiemer, S., & Wyss, M. (2000). Minimum Magnitude of Completeness in Eartquake Catalogs: Example from Alaska, the West United States, and Japan.

Woessner, J. (2005). Assessing the Quality of Earthquake Catalogues: Estimating the Magnitude of Completeness and Its Uncertainty. *Bulletin of the Seismological Society of America, 95*(2), 684-698. doi: 10.1785/0120040007